Rotation curves of mock EAGLE dwarf galaxies vs simulations

MARIA MARGARITA LUNA-GARCIA

Rotation curves of mock EAGLE dwarf galaxies vs simulations

Margarita Luna Garcia

A thesis presented for the degree of
Master of Science

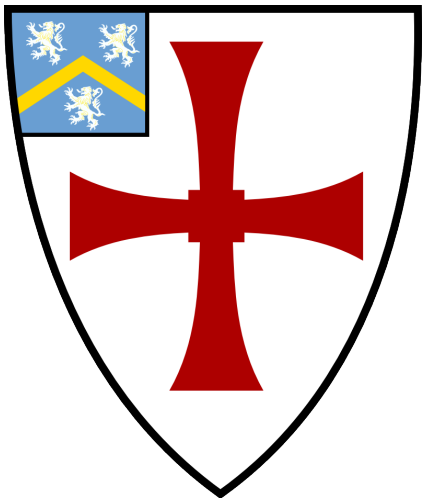

Centre for Extragalactic Astronomy
Institute of Computational Cosmology
The University of Durham
United Kingdom

December 2022

Rotation curves of mock EAGLE dwarf galaxies vs simulations

Margarita Luna Garcia

Abstract

The dark matter mass distribution within galaxies has been the subject of extensive studies, leading to the cusp/core problem as one of the main topics of discussion. Mock observations provide a way to bridge the gap between simulations and observations by understanding the source of this discrepancy. In this thesis, we create mock observations of the stellar component of dwarf galaxies from two runs of the EAGLE simulations with different star-formation gas density thresholds, a low threshold (LT) and a high threshold (HT). We use SimSpin to make the observations, and define the observing parameters as those from the MUSE instrument with a redshift of 0.2. The galaxies are observed both with and without atmospheric seeing conditions i.e. a point-spread-function (PSF) convolution of $0.3''$. The kinematics of these galaxies are obtained through GIST, which fits the spectrum of the integral field unit cube and recovers the velocity at each pixel. From the line-of-sight velocity map, we select a slit two pixels wide and recover the rotation curves, which we compare directly with the input EAGLE particle data using a slit of the same size. We find dissimilarities between the two as a result of the fitting routines, which are emphasized by the differences caused by the star formation gas density threshold on the structures of the galaxies. HT galaxies have less ordered rotation which leads to less pronounced absorption lines to be used for the spectrum fit and lower velocities, hence, we find larger discrepancies between the rotation curves at HT than at LT. We attempt different methods of processing one LT galaxy, such as removing the PSF convolution, reducing the signal-to-noise ratio, and changing the spectral template, but the discrepancies remain. In particular, we compare the maximum and the fiducial velocities for the mock observations using the radii from EAGLE and the input EAGLE data and find differences between the two as a result of the choice of radii. In general, the differences between the mocks and EAGLE are not seen across all galaxies, but rather in the sample as a whole. This study demonstrates how we can use instruments such as SimSpin to study the role of observational biases in the study of stellar kinematics.

Supervisors: Dr. Anna McLeod, Dr. Azadeh Fattahi, and Dr. Annagrazia Puglisi

Acknowledgements

The completion of this thesis would not have been possible without the consistent support of my supervisors: Anna McLeod, Azi Fattahi and Annagrazia Puglisi. Thank you for your feedback, your help, and your time.

Contents

Chapter 1

Introduction

In the study of galaxy formation and evolution, there are two main routes: performing simulations or gathering observations. Both methods can give us an insight into the formation and evolution of galaxies, where simulations can create large samples of galaxies from a set of initial conditions and see the way they evolve within a large range of properties, whereas observations can reveal a snapshot of their true structure. Observations have limitations as a result of instrumental resolution, noise contamination, and sample size; similarly, cosmological simulations have limitations since a single particle must account for multiple solar masses worth of stars, gas, or dark matter (DM). Additionally, sub-grid physics prescriptions for star formation and stellar feedback can lead to a large number of parameters which imply degeneracies. Therefore, to validate the results of simulations and confirm our understanding of galaxy evolution, there is a need to compare predictions from simulations with observations of galaxies. One of the most direct ways to perform such comparisons is by making mock observations of observables from simulations, which will be the main focus of this dissertation. An emphasis will be placed, particularly, on the kinematics of galaxies and the ability of mock observations to recover the rotation curves of simulated galaxies. The kinematic properties from mock observations will be compared with previous mock observations and the kinematics of dwarf galaxies directly from the output of simulations. The rotation curves will be used to study the dark matter radial distribution in dwarf galaxies, which has been a topic of intense debate within the community and is the motivation for this research project.

1.1 The cusp/core problem

One of the first pieces of evidence of the existence of dark matter came from observations of galaxies in a galaxy cluster. In 1933, Zwicky (1933) studied the velocities of galaxies in the Coma cluster and determined that the luminous matter in each galaxy –mostly composed of stars– was not enough to keep the cluster together. Within the next few decades, further proof of the existence of some type of matter that only interacted gravitationally came to light; this was evidenced through gravitational lensing effects, the orbits of satellite galaxies, and galaxy rotation curves (Tyson et al., 1990; Ostriker et al., 1974; Roberts & Rots, 1973). These observations provided proof of the existence of dark matter haloes: large, gravitationally bound objects that surround galaxies and make up most of the matter within a galaxy and in the universe. When observing galaxies, some evidence of the existence of dark matter came from the rotation of the disk of spiral galaxies, particularly from stars and hydrogen clouds. The circular velocity, $V_{\rm circ}$, can be used to approximate the total mass enclosed within a certain radius (Roberts & Rots, 1973). Initial observations determined that there was not enough visible matter to support the velocities found at large distances from the centre of the galaxy, which left dark matter as an explanation for the lack of visible matter. This led to the theory that dark matter is distributed throughout a galaxy and that it extends radially beyond the gas of a galaxy, forming a halo. The total dark matter halo mass, $M_{\rm halo}$, is defined in this work as the mass contained within the virial radius. In a toy model of how halos form, the halo has reached a point of equilibrium at the virial radius, where particles beyond this point will not be gravitationally bound to the system. This equilibrium is known as the point of overdensity, which usually occurs when the density is 200 times that of the average density of the universe, and it dictates the radial extent up to which the halo is in equilibrium and the mass enclosed within that radius. The virial mass, velocity, and radius are defined as M_{200}, V_{200}, and r_{200}, respectively, where:

$$M_{200} = \frac{V_{200}^2 r_{200}}{G}, \tag{1.1}$$

and G is the gravitational constant. Equation 1.1 uses a spherical approximation, which can be applied to determine the density within different spherical shells up to the virial radius. The density of all of these shells can be added to find the density profile of the dark matter halo.

Dark matter halo models favour a triaxial shape that extends beyond the galaxy's baryonic edge and a density distribution that changes with radius. Navarro et al. (1997) used dark matter only (DMO) simulations to develop the Navarro, Frenk &

White (NFW) density profile, where the density $\rho(r) \propto r^{\alpha}$, where r is the radius from the centre of a galaxy, and α changes from the centre to the outskirts of a galaxy. Approaching $r = 0$ kpc, $\alpha = -1$, but further away, $\alpha = -3$, meaning that the density is steeply increasing towards the centre of a galaxy and forming a cusp, and declining as the distance from the centre increases, up to the virial radius. Or, in terms of the circular velocity, it is steeper near the centre and $V_{\rm circ} \propto r^{1/2}$. In DMO simulations, this relation can be applied to model the halo of a galaxy of any size, where the halo of a dwarf galaxy is indistinguishable from that of a cluster when scaled to the characteristic density and radius (Navarro et al., 2004). However, a problem lies in the deviations seen when looking at specific haloes. Large spiral galaxies have a central density dominated by baryons, which changes the mass distribution of the DM from NFW. Additionally, observing the DM density distribution within the inner radius of a halo becomes more difficult due to their bright central bulge, where beam smearing affects the measurements of the rotation velocity of the galaxies. Dwarf spiral galaxies and low surface brightness (LSB) galaxies become the ideal hub for observations since DM is expected to dominate even at their centre, in contrast to spirals and ellipticals which have baryon-dominated cores. As a result, dwarf and LSB galaxies have a stellar mass to halo mass ratio, $M_*/M_{\rm halo} \approx 10^{-2} - 10^{-3}$. In addition, they have enough visible matter that it is possible to map out their rotation curves. Moore (1994) measured the rotation curves of four dwarf galaxies with a stellar mass, $M_* \approx 10^8 M_{\odot}$ and found that, at $r < 4$ kpc, the rotation velocity of disk galaxies rises linearly with radius, which, according to Equation 1.1, indicates that $M \propto r^3$ and therefore the density is constant ($\propto r^0$). This constant density implies that the density slope of the halo's centre is shallower than predicted by NFW, and that the velocity rises linearly with radius, $V_{\rm circ} \propto r$. This is known as the cusp/core problem, where, from observations we can infer the presence of a core while simulations provide evidence of a cusp. The problem could be due to several characteristics: observational shortcomings such as beam smearing, degeneracies between luminous and dark matter which become important at these scales, feedback effects, and DM particle properties. Even though baryonic matter only makes up ∼15% of the matter in the universe (Planck Collaboration et al., 2020), at the centre of large galaxies, the baryonic matter is denser than the dark matter. At the centre of dwarf galaxies, DM often dominates, but feedback events can disrupt the mass distribution, so any changes in the baryons can affect the DM as well (Bullock & Boylan-Kolchin, 2017). The main contributors to this change are stellar winds, supernovae, and Active Galactic Nuclei (AGN), which drive a change in the M_* to $M_{\rm halo}$ ratio of the galaxy. This, in turn, depends on the size and environment of the galaxy; the main category that will be explored is dwarf galaxies.

Larson (1974) quantified the amount of gas lost in a galaxy as a result of supernovae and found that dwarf galaxies lose a significant amount of gas through this process. Navarro et al. (1996) suggested that during the formation of the disk of a bright dwarf galaxy (i.e. within a stellar mass range of $M_* \approx 10^7 - 10^{10} M_\odot$, or $M_*/M_{\rm halo} \approx 10^{-3} - 10^{-2}$), supernovae are expected to drive large scale winds that drive out baryonic matter. The DM halo, which had compressed and settled into equilibrium, is affected by the removal of the disk potential by the winds. The oscillations in the potential add energy to the DM particle orbits, which leave the particles unbound, so they leave the centre of the halo, making these systems less cusped (Pontzen & Governato, 2012). In larger, more bound systems, AGN feedback becomes more relevant. The removal of DM through AGN feedback is similar to that of supernovae: the processes around the central supermassive black hole heat the surrounding gas and transport the gas out of the centre of the system, changing the central potential and the orbital energy of the dark matter, causing its expansion(Bower et al., 2017; Peirani et al., 2019). At lower stellar masses, $< 10^7 M_\odot$, galaxies do not have enough stars to create the necessary supernovae energy to drive a significant change in the potential well of the halo (Garrison-Kimmel et al., 2013). Simulations which include baryonic feedback show varying results given that different feedback implementations are employed and different variables are used to calibrate the simulations, for example. Lazar et al. (2020) found a relationship between the density slope close to the centre, α, and the stellar to halo mass ratio ($M_*/M_{\rm halo}$) using the FIRE simulations. At the maximum α, galaxies are most efficient at driving out dark matter from the halo centre through stellar feedback. This peak is reached when $M_*/M_{\rm halo} \approx 5 \times 10^{-3}$ and $M_* \approx 10^8 M_\odot$, resulting in a density slope of $\alpha \approx -0.1$. Below and above this ratio, the density distribution is steep in this simulation. Lazar et al. (2020)'s analysis, however, only produces cores in a small range of masses, and it does not consider the diversity of rotation curves or the density profiles seen in actual observations. This diversity was considered by Oman et al. (2015) in their study of dwarf galaxy rotation curves from the EAGLE simulations (see Sect. 2.1). Some simulations can accurately reproduce observed properties of galaxies without necessarily producing a core, such as EAGLE (Schaye et al., 2015), APOSTLE (Sawala et al., 2016) and Illustris (Vogelsberger et al., 2014), showing that different recipes for feedback can easily affect the dark matter distribution.

Oman et al. (2015) compared the rotation curves of galaxies from the EAGLE and APOSTLE simulations with those of observations and looked at the relationship between the circular velocity at 2 kpc from the centre, $V_{2\ \rm kpc}$, and the maximum velocity reached by the rotation curve, $V_{\rm max}$, as shown in Fig. 1.1. The figure shows data from EAGLE and APOSTLE (Sawala et al., 2016; Fattahi et al., 2016)

simulations from DMO runs, hydrodynamical runs, and data from observations. They found that simulations have a much smaller scatter in the values of $V_{2\ \mathrm{kpc}}$ per V_{max}, compared to observations. $V_{2\ \mathrm{kpc}}$ can span a range of more than a factor of ~ 4, meaning that on one extreme, at 2 kpc some galaxies have a circular velocity comparable to its maximum velocity. Therefore, they should have an enclosed mass double its baryonic mass, and on the other, some galaxies have lost enough DM mass comparable to their total baryonic mass. For simulations, V_{max} can be used to infer the distribution of the dark matter mass within a galaxy, which can be used to compare the mass profile with observations by finding the observed maximum velocity. When extracting the velocities from observations, the disentanglement of the contributions due to baryonic mass versus dark matter mass is model-dependent, which leads to uncertainties in the recovery.

1.2 Integral Field Spectroscopy

Lately, Integral Field Spectroscopy (IFS) techniques have evolved to provide a deeper view into the structures, histories, and properties of galaxies, including dwarf galaxies. Integral Field Unit (IFU) cubes create a 3D view of a galaxy. They have a spatial 2D component and a spectral 1D component, which allows for a kinematic study of the gas and stellar components of a galaxy. For each pixel in the image, you can get a spectrum and hence use the central peak of the absorption lines to find the velocity of the region. Many IF spectrographs have been developed, such as GMOS (Allington-Smith et al., 2002), VIMOS (Le Fèvre et al., 2005), BOSS (Smee et al., 2013), PMAS/PPAK (Kelz et al., 2006), SAURON (Bacon et al., 2001) and MUSE (Bacon et al. 2010, see also Sect. 2.3). These instruments have completed large surveys of hundreds to thousands of galaxies within the optical and near-infrared wavelength range, surveys such as ATLAS^{3D} (Emsellem et al., 2011), CALIFA (Sánchez et al., 2016a), SAMI (Scott et al., 2018), and MaNGA (Bundy et al., 2015) which are publicly available. IFS has multiple uses in the study of galactic evolution and formation, and several tools have been developed to understand the stellar and gas kinematics, star formation histories, and properties of the local and global stellar population using IFS (Cappellari & Emsellem, 2004; Cid Fernandes et al., 2005; Sarzi et al., 2006; Koleva et al., 2009; González Delgado et al., 2015; Sánchez et al., 2016a, and more).

With the extent of information that can be learnt, there are also drawbacks in the complexity of the data analysis necessary to understand the observed data. For example, when performing ground observations, the Point Spread Function (PSF) causes degradation of the observations due to atmospheric seeing conditions,

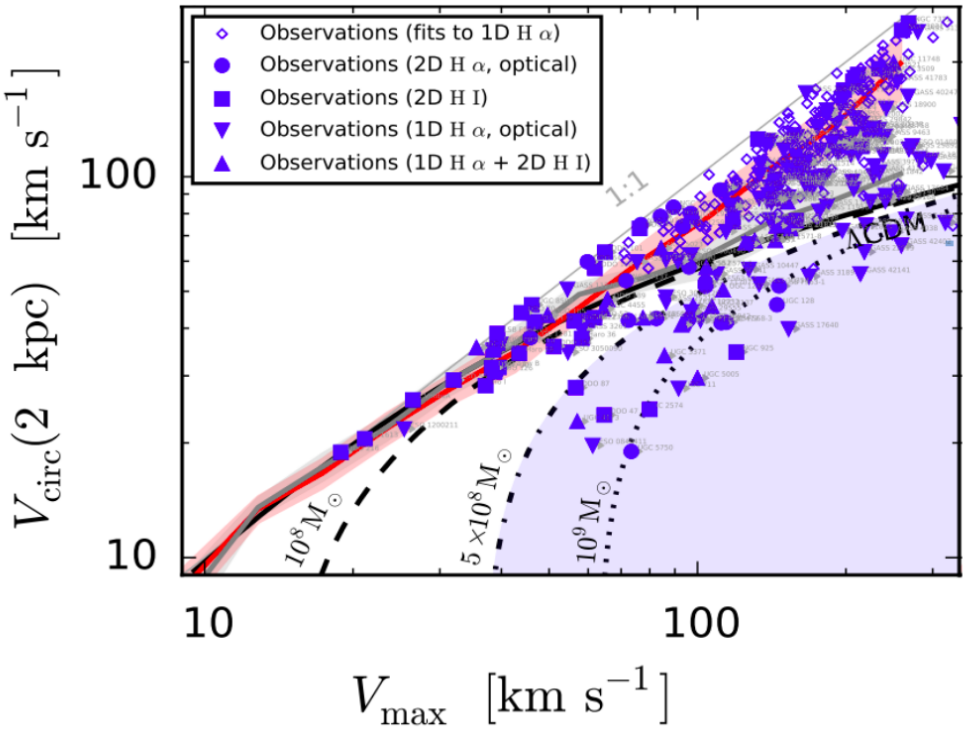

Figure 1.1: Circular velocity at $r = 2$ kpc versus the maximum circular velocity, $V_{\rm max}$, of observed and simulated galaxies (adapted from Oman et al. (2015)). The relationship for EAGLE and APOSTLE simulated galaxies is plotted as a solid grey line for dark matter only (DMO) runs and in red for hydrodynamical runs, with the shaded area of the same colours denoting the standard deviations. Observations of galaxies whose inner structure can be resolved below 2 kpc are plotted as the blue symbols, with each shape denoting a different tracer observed, such as HI, Hα, optical, and whether the observations are in 1D or 2D, as indicated in the legend. The dashed black lines display the amount of mass that would need to be removed within the inner 2 kpc to form a curve with that shape. There is a larger scatter in the values of $V_{\rm circ}(2$ kpc) per $V_{\rm max}$ in the observations than in the simulations, showing there is a larger diversity in the rotation curves observed.

aberration from the telescope and instrument, and the sampling size. These effects limit the spatial information unless corrected using Adaptive Optics (AO), which reduces the Full-Width-at-Half-Maximum (FWHM) of the PSF. PSF degradation effects have the potential to alter the process of mapping the rotation of a galaxy as we approach its centre, which becomes complex since velocities reach zero rapidly and the luminosity increases. The rapid change leads to large uncertainties and inferences on the velocity distribution, which could drastically alter the inferred rotation curve of a galaxy, which, in turn, affects the accurate recovery of the dark matter distribution. There are forward modelling techniques used to correct for the PSF and to extract information from IFU cubes, such as ^{3D}BAROLO (Di Teodoro & Fraternali, 2015) and GalPaK (Bouché et al., 2015), that, while greatly improving kinematic measurements, have a large number of parameters and hence large degeneracies in the results. The tools depend on an approach to describe the kinematics of a galaxy, such as the tilted-ring model (Rogstad et al., 1974).

Some tools have been created for the purpose of data reduction and analysis of IFU cubes. Some of these pipelines are Pipe3D (Sánchez et al., 2016b), LZIFU (Ho et al., 2016), the MaNGA pipeline (Westfall et al., 2019), and GIST (Bittner et al., 2019) (see Section 2.6). They extract spectral information and properties of stellar populations from IFS data using spectral templates and other fitting routines. In this case, we used GIST, an all-in-on framework designed for use on MUSE data but can also be applied to data from other IFS instruments.

One way to test the reliability of a tool such as GIST and the rotation curve extraction methodologies from IFU data, is to perform the same processing methods on mock observations of cosmological hydrodynamical simulations of galaxy formation. Simulations have information known a prior; therefore, processing the data with a specific pipeline allows for the evaluation of systematics in these tools. Recent simulations have reached levels of complexity similar to real galaxies, and there is a need to create mock observation and analysis tools which match those results. Multiple pipelines have been designed to produce mock observations by replicating the observing effects of a specific instrument. These pipelines have been used to study the role of the different parameters involved in making observations, and how they compare with the original simulations. For example, Kendrew et al. (2016) studied the stellar kinematics of high redshift galaxies using HSIM (Zieleniewski et al., 2015) to produce mock observations, replicating the HARMONI instrument (Thatte et al., 2014). Nanni et al. (2022) developed iMaNGA to produce mock observations of the Illustris (Nelson et al., 2015) and IllustrisTNG (Nelson et al., 2019) simulations to compare with the MaNGA survey (Bundy et al., 2015). Guidi et al. (2018) created SELGIFS to generate mock IFS data mimicking the CAL-

IFA survey (Sánchez et al., 2016a). Finally, SimSpin can be applied to multiple hydrodyanamical simulations and can mock observe with various IFU instruments (Harborne, 2019) (see Sect. 2.4). There are still underlying systematic differences that need to be taken into consideration when making mock observations, such as intrinsic problems in the hydrodynamical simulations and the techniques used to create the spectral population templates, however mocks still provide a way to understand more closely the data analysis methods used.

1.3 Goals of this study

In this work we analysed two runs from the EAGLE simulations; one run used the fiducial galaxy formation parameters described in Schaye et al. (2015), and the other run applied a higher star formation density threshold (Benítez-Llambay et al., 2019). Roper et al. (2022) studied the rotation curves of galaxies from these two EAGLE runs using the atomic gas. In this work, the stellar particle data from selected galaxies within those runs were mock observed using SimSpin: both with and without a PSF to understand the accuracy of SimSpin mock observations. After creating the observations using SimSpin, they were processed with GIST to extract the kinematic data, and then used a slit to obtain the rotation speeds. The rotation was compared with that from the raw EAGLE particle data, which was extracted in a similar way. We used two runs of EAGLE with different star formation thresholds since it allowed us to understand how galaxies with different structures can affect the accuracy of the output from mock observations hence our ability to recover the rotation speeds. SimSpin does not currently produce mock observations of the gas, so we used solely the stellar particle data, which allowed us to understand the role of the stellar kinematics of dwarf galaxies in the dark matter distribution.

We begin by describing the EAGLE simulations, and the methods used to select the galaxies in Chap. 2, which leads to a depiction of SimSpin and its use in producing mock IFU cubes of MUSE. We compare the mock observations with EAGLE and analyse the role of PSF convolving in Sect. 2.5, then we describe GIST and the selection of rotating galaxies in Sect. 2.6. In Chap. 3, the rotation curve extraction from both GIST and EAGLE are described, as well as the impact of PSF convolving on the rotation curves. We explore the differences seen for one particular galaxy in Sect. 3.3, and the overall differences between the inner and outer velocity in Sect. 3.4. Finally, the implications of our findings and further developments of this work are summarised in Chap. 4.

Chapter 2

Methods

2.1 The EAGLE Simulation

The EAGLE project is a suite of hydrodynamical simulations (Schaye et al., 2015) coming from a modified version of the GADGET-3 code: an N-body, Tree-PM Smoothed Particle Hydrodynamical code. The simulations include radiative cooling, star formation and stellar feedback, stellar mass loss, Active Galactic Nuclei (AGN) feedback, gas accretion and mergers of supermassive black holes (SMBHs). These simulations follow the formation of galaxies and are calibrated according to observations of the galaxy mass and size function (Baldry et al., 2012; Li & White, 2009; Shen et al., 2003), and the stellar mass to SMBH mass relation (McConnell & Ma, 2013). The runs used for this dissertation project were originally performed by Benítez-Llambay et al. (2019) inside a volume with sides of 12 Mpc, 256^3 dark matter particles, a dark matter particle mass resolution of 3.2×10^6 $M_\odot$, and a gas and stellar particle mass resolution of 5.3×10^5 $M_\odot$. One run uses the same parameters as the fiducial EAGLE-recal, which reproduces the calibrated parameters, whereas the other differs from the EAGLE-recal run in the change of star formation density threshold ($n_{\rm th}$):

$$n_{\rm th} = \min[n_{\rm min}(\frac{Z}{Z_0})^{-\alpha}, n_{\rm max}]. \tag{2.1}$$

This parameter is evaluated as a mass density rather than a hydrogen number density and it is metallicity-dependent (Schaye et al., 2015; Benítez-Llambay et al., 2019). For simplicity, the threshold was fixed at $\alpha = 0$, $Z_0 = 0.002$, and $n_{\rm min} = n_{\rm max}$ for these runs. By changing this threshold, properties of galaxies change, such as the gas mass, the stellar mass, the star formation rate, the age, etc.... (Pontzen & Governato, 2012; Shen et al., 2014; Burger et al., 2022). Overall, the way the galaxies evolve is altered by this threshold, and one particular effect which was explored is the effect on the dark matter density distribution.

The two runs used in this analysis are the low and high thresholds (LT and HT, respectively), where LT = 0.1 cm^{-3} and HT = 10 cm^{-3}. At the low threshold, also known as the fiducial run, the galaxy properties match the observed calibration properties described before in addition to other observables, such as the rotation curves, which were analysed in this dissertation. At the high threshold, Benítez-Llambay et al. (2019) produced cores of constant density close to the centre of a galaxy, unlike the runs at LT. The threshold of 10 cm^{-3} was selected for this analysis since galaxies at HT resemble those from LT, and therefore observations, closely. Galaxies from runs with values above HT bear little resemblance to actual dwarf galaxies; these galaxies are extremely HI rich, almost a dex above observations (and the fiducial run), for that reason they were not included in this analysis. Higher thresholds than HT have been used in other simulations (such as the FIRE-2 simulations of Fitts et al. (2017)) and these have been able to produce cores. Higher thresholds tend to have more bursty star formation events, driving rapid changes in the gravitational potential of the galaxies and, therefore, removing dark matter from the centres of galaxies. The fiducial EAGLE run, meaning the run at low threshold, on average, failed to develop cores in the density profile since enough gas was allowed to accumulate and get dense enough that in some small regions they dominate the gravity, allowing star formation events to remove large amounts of gas and therefore dark matter. However, both LT and HT are far below the density at which stars have been observed to form, approximately $n_{th} = 10^4$ cm^{-3}(Dutton et al., 2019). This is observed at smaller scales than what these simulations can resolve. Other studies argue that changing n_{th} is not necessary for the formation of cores or that it might not be enough to alter n_{th} in simulations (Jahn et al., 2021; Benítez-Llambay et al., 2019; Dutton et al., 2020). Here, we are not testing the accuracy of the results but comparing the fidelity of a method of making mock observations, and the methods used to extract information such as the rotation curves dwarf galaxies, which are used to derive the mass distribution.

EAGLE defines a galaxy through the use of the Fiends of Friends (FOF, Davis et al., 1985) and the SUBFIND (Springel et al., 2001; Dolag et al., 2009) algorithms. Initially, FoF defines a dark matter halo by grouping the dark matter particles which lie at a shorter distance than 0.2 times the mean interparticle separation, measured by averaging over the entire box. Particles are added to this halo until it reaches an overdensity value of approximately the average virial overdensity of 180, i.e. the value predicted in the Einstein-de-Sitter cosmology model (Einstein & de Sitter, 1932). FoF then groups the gas and stellar particles according to the group of the nearest dark matter particle. SUBFIND then defines the substructure by finding the peaks in density within the halo, grouping the stellar, gas, and dark matter particles within that region, and defining them as subhaloes. The subhalo

that carries the dark matter particle with the minimum gravitational potential becomes the central galaxy, and the location of this particle is also used to define the centre of the galaxy. The centres of the satellite galaxies are defined as the other points of minimum potential. Particles which are not gravitationally bound to the structure are removed from the group. Following this removal process, EAGLE still identifies some galaxies as part of the same group if they are going through a merger event and are therefore bound by gravity. However, in this study, we only considered isolated, non-merging galaxies because these events alter the kinematical structure of the galaxy. We perform further selection cuts throughout the process, such as removing galaxies which are not the group's central galaxies, do not have a clear rotation, or clusters of stars without dark matter.

2.2 Sample selection

The galaxies analysed in this thesis were originally selected from the simulations by limiting the stellar mass range from 10^7 to 10^{10} $M_\odot$, or approximately 10^2 to 10^5 stellar particles per galaxy. The mass of a galaxy is defined as the sum of the mass of the particles within the virial radius of a galaxy. This mass range lies within the dwarf galaxy regime, where we expect stellar feedback to have large effects on the dark matter mass distribution, as mentioned in Chap. 1. Smaller galaxies lose a significant amount of gas through stellar winds and supernovae, which drive large-scale winds that drive out baryonic matter. These stellar feedback events affect the mass distribution of low-mass galaxies, which can be observed through their rotation curves. Steeply rising circular velocities indicate that there is a large amount of mass close to the centre of the galaxy i.e. dark matter which has not been removed by feedback events (Benítez-Llambay et al., 2019). This difference is visible in the low and high thresholds, where the amount and the frequency of star formation events changes, which leads to differences in the mass distribution of a galaxy and, therefore, varying rotation curves. This difference enables a comparison between the impact of feedback on the mass distribution, which should be distinguishable in the outcome from mock observed galaxies. Galaxies with clear rotation are necessary to ensure that the kinematics are not being perturbed by other effects (such as interactions). To derive this rotation, the simulations were processed in the following way.

The same mass selection cuts were applied for both thresholds, resulting in a sample of 86 galaxies at LT and 72 galaxies at HT. Each LT galaxy has a HT counterpart, which can be found given that both runs have the same dark matter particle IDs, which allowed us to match the dark matter halos and their host galaxies for both

runs. This allowed for a comparison between the output from both runs, where the only difference is due to the change in star formation gas density threshold.. Fig. 2.1 shows the stellar mass, M_*, to dark matter halo mass, M_{200}, relation of the galaxies compared to the expected stellar-to-halo-mass relation (SHMR) from Behroozi et al. (2013). The galaxies in the LT run have a higher stellar mass per DM mass than HT, additionally there are fewer galaxies at the higher mass end, which is expected given the stellar mass function, where the number density of galaxies declines at the higher mass end (Baldry et al., 2012). Fig. 2.2 (left) shows the relationship between the gas mass, $M_{\rm gas}$, and M_* for each galaxy at both HT and LT. At the higher stellar mass end, HT galaxies have a higher gas mass than LT galaxies, meaning that although feedback events are able to form cores and the galaxies have enough gas mass to disrupt the gravitational potential and hence redistribute the dark matter, a lot of the gas mass remains within the galaxies, more than at LT, which can change the structure of the galaxy. At the lower stellar mass end there is more scatter in the data where, on average, both LT and HT galaxies have similar gas masses. However, Fig. 2.2 (right) shows the baryonic mass to dark matter halo mass relationship, where the total baryonic mass ($M_{\rm bar}$) remains nearly constant for both LT and HT, meaning that the gas which is not being used for star formation at the high threshold still remains within the galaxy. The total baryonic mass includes the gas mass and the stellar mass of each galaxy.

2.3 MUSE IFS data

The Multi-Unit Spectroscopic Explorer (MUSE, Bacon et al. (2010)) is an Integral Field Spectrograph mounted on the Very Large Telescope at the European Southern Observatory. The instrument runs on two modes: the Wide Field Mode (WFM) that covers a field of view of 60"×60" with a spatial sampling of 0.2"×0.2" and the Narrow Field Mode (NFM), that spans $7.5'' \times 7.5''$ with a spatial sampling of $0.025'' \times 0.025''$. It observes in the optical range within $4650 - 9300$ Åand it can operate with adaptive optics to reduce the effects of atmospheric seeing. MUSE has been used to study the rotation curves of galaxies both at high and low redshifts and their resulting dark matter profile (Guérou et al., 2017; Tiley et al., 2019; Bouché et al., 2022; den Brok et al., 2020).

2.4 Building mock IFU cubes

For this analysis, we consider the stellar particle data since SimSpin is only able to process stellar particle data. Roper et al. (2022) looked at the gas particle

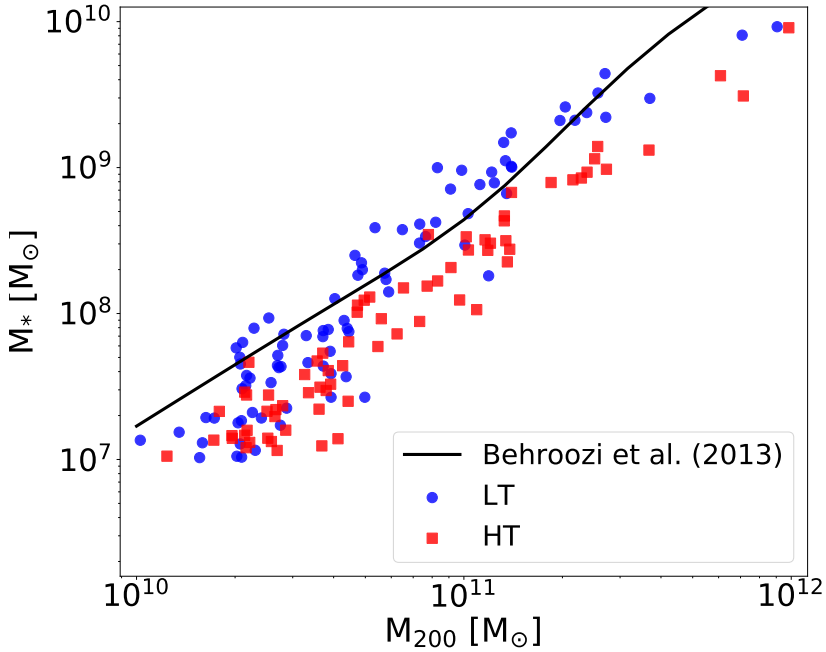

Figure 2.1: Stellar to dark matter halo mass plot of selected EAGLE galaxies with stellar masses within 10^7 to 10^{10} $M_\odot$. The plot shows both LT galaxies (blue circles), HT galaxies (red squares), and the stellar-to-halo-mass relation (SHMR) from Behroozi et al. (2013) (black solid line). The LT galaxies tend to follow the SHMR, while HT galaxies underestimate the expected stellar mass content.

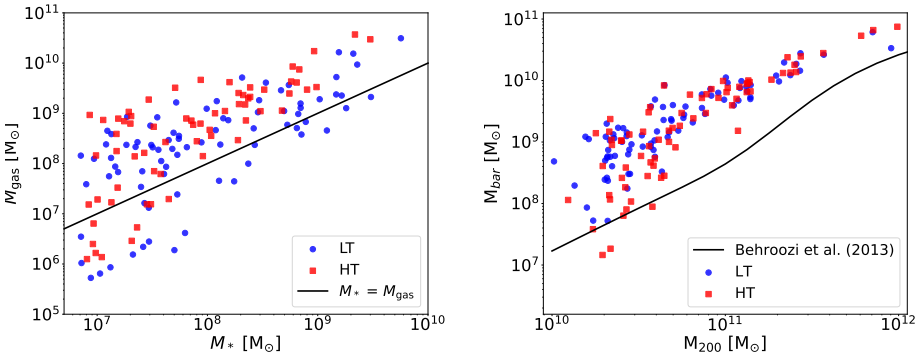

Figure 2.2: *Left:* Stellar mass to gas mass plot of selected EAGLE galaxies with stellar masses within 10^7 to 10^{10} $M_\odot$. The plot shows both LT galaxies (blue circles) and HT galaxies (red squares) and the 1:1 relation (black line). At the higher stellar mass end, HT galaxies have a higher gas mass than LT galaxies, while at the lower mass end, there is more dispersion. *Right:* Baryonic mass to dark matter halo mass of the same sample of galaxies. The colour coding is as in the left-hand figure, with Behroozi et al. (2013) as a reference line in black showing the SMHR. The plot shows that the total baryonic mass remains the same for both LT and HT galaxies.

data for EAGLE galaxies in the dwarf galaxy mass regime at the two thresholdsm, and mock observed the galaxies using ^{3D}BAROLO and the tilted-ring model (Di Teodoro & Fraternali, 2015). They found that the methods used to create the mock observations were not able to replicate the cores seen in the circular velocity from the HT galaxies, although they were expected to be there. They argue that the rotation curves are affected by non-circular motions of the gas and the gas disk thickness, which washes out the signature of the cores. By looking at the stellar particles we can test whether the same is true for stars.

Each stellar particle within the selected galaxies from EAGLE has its own information, such as the initial stellar mass, age, metallicity, velocity, and position. These parameters are used to make the mock IFU cubes. These cubes are created using SimSpin (Harborne, 2019), a software which takes in stellar population particle data from N-body or hydrodynamical simulations and creates mock IFU cubes. The parameters taken from the simulations are used by SimSpin in different ways. SimSpin requires the initial stellar mass, age, and metallicities of the stellar particles to fit a Single-Stellar Population model (SSP) and build the Spectral Energy Distribution (SED) of a galaxy, meaning the expected spectra of each particle given the characteristics of the stellar populations in that region. In this work, we are using EMILES (Vazdekis et al., 2016) due to the high resolution of the template and the extensive types of stellar populations and wavelengths used to make the template. The EMILES library spans the metallicity range -1.79 $<$ [M/H] $<$ 0.26, stellar ages above 30 Myr, and spans a wavelength range of 1680 to 50000 Å, which is ideal for this analysis since MUSE observes in the optical range, i.e. within 4700 - 9351 Å.

Once the spectral data for the particles is built, a constant signal-to-noise ratio of 10 per pixel is applied, which was maintained constant for all observations. Skylines are not added by SimSpin, therefore the noise comes from a random normal distribution of values with a mean at zero and one standard deviation wide. Additionally, the spectra was convolved with a Gaussian line-spread-function (LSF), which has a constant FWHM of 2.63 Å over the entire wavelength range. The particles' locations depend on the point at which the observer is placed; to determine the POV, SimSpin allows the user to set the inclination angle of the galaxy and the twist angle, i.e. the side from which the galaxy is viewed. At an inclination of 90°, the galaxy is viewed edge-on while at 0° it is viewed face-on. The galaxy can be twisted 180° along the z-axis. SimSpin also centres the galaxy based on its centre of mass and determines the plane based on the inertia tensor of the galaxy and its eigenvectors. For the galaxies which are not rotating along a disk plane, the best estimate for this plane is used; however, during the post-process, these

Parameter	Value
IFU field of view (″)	15
Wavelength range (Å)	4700−9351
Spatial resolution (″)	0.2
z	0.2
Inclination (°)	90 (edge-on)
PSF FWHM (″)	0.3

Table 2.1: Mock IFU data parameters.

galaxies were removed from the sample. To find the disk plane, SimSpin first determines the shape of the galaxy. It does so by iterating until the ratio between the major and minor axes of an ellipse converge to a value equal to the previous ten iterations and fit the galaxy, then finds the total mass within the ellipse to determine the half-mass radius, which the code uses to select the particles lying within this radius. The plane of rotation is shifted according to the eigenvectors and eigenvalues until the galaxy is rotating about the z-axis. The code only includes the particles within the half-mass radius since it reduces the rotation scatter coming from the stars further away from the centre. We set the inclination to 90° (edge-on) to minimise the uncertainties due to inclination correction in the analysis and enable a more direct comparison with the EAGLE rotation curves.

Once the galaxies have been centred and rotated by SimSpin, it applies the parameters of observation depending on the telescope adopted. These parameters are the spatial resolution, field of view (FOV) and its shape, among others, also described in Table 2.1. We use MUSE, where the default settings have been applied, such as a square aperture, a spatial sampling of 0.2″ per pixel, and a field of view of 15×15 arcsec. Although MUSE has a FOV of either 1×1 arcmin or 7.5×7.5 arcsec, we choose 15×15 arcsec and a spatial sampling of 0.2″ due to the reduced computational time. In order to determine the size of the projection of the galaxy in the sky, a redshift of 0.2 was also selected, such that the full extent of the galaxies was visible within the FOV. In order to replicate observational constraints, SimSpin can mock-produce "beam smearing" effects by convolving each spatial plane with a PSF. In the case of MUSE, the highest spatial resolution is of 0.3″ with adaptive optics (AO), but values can usually range from 0.3″ to 1″ without AO depending on the atmospheric conditions. For this analysis, the highest resolution has been applied, meaning a PSF with a gaussian shape and a FWHM of 0.3″ was convolved with the flux in each pixel along each plane.

Fig. 2.3 shows examples of mock IFU cubes which have been collapsed. To collapse the cubes, the emission at every spaxel was added up over the MUSE range of

wavelengths to obtain the full emission of the galaxy. This is shown for a LT galaxy (LT10213, top) and its HT counterpart (HT10712, bottom), both PSF Convolved (Conv) and non-convolved (Free) (left and middle column), created using the parameters of observation mentioned above. These two galaxies were matched from the dark matter particle IDs, which remained constant on both runs. LT10213 is a LT galaxy with a stellar mass of 4.4×10^9 $M_\odot$, and HT10712 is a HT galaxy with a stellar mass of 1.4×10^9 $M_\odot$. On the right, the residuals of Conv−Free are displayed, with the values of flux ranging from -10^{-6} to 10^{-6} erg cm^{-2}s^{-1} . From Fig. 2.3, a difference between these two thresholds is clear on both the Conv and Free image, where there are peaks of brightness in the HT galaxy which occur further from the bulge. The galaxy is also less disk-like, unlike LT which has a central bright bulge and thin disk. The difference in structure shows that star formation events could be disrupting the disk of HT, where the repeated perturbations prevent the formation of a cusp in HT galaxies (Benítez-Llambay et al., 2019). The residual plot shows that there are differences between the convolved images and the Free images, where LT reaches peaks in flux in the centre for both Conv and Free, but Conv is dispersing this luminosity and adding it to nearby pixels, therefore, we do not see a smooth residual bulge and thin disk. For HT, the residuals show a smoother distribution towards the centre, where the highest luminosity peaks are still being underestimated through the process of convolution. Outside the central bulge, the difference in flux is close to zero.

2.5 SimSpin and EAGLE comparison

From the photometric and spectroscopic infromation of these mock IFU cubes, information about the stellar kinematics of a galaxy can be derived in order to study the physical processes that influence the kinematics, and the fidelity of mock observations in reproducing simulated data. Before processing the kinematics, we directly compared the output from SimSpin and the input data from EAGLE. At this stage, the collapsed cubes were used to determine where the half-light radius lies and compare this with the half-mass radius from the input data. We placed an aperture centred on the galactic centre of the collapsed cubes, with a radius which started from the centre of each galaxy, and grew with every pixel until the full $15'' \times 15''$ square could fit within the aperture (or $\sim 50 \times 50$ kpc). The centre of the galaxy was determined by SimSpin and taken to be the central pixel. The flux of the entire galaxy, f_{total}, was added and halved to find the radius at which half of the stellar light is being emitted, $R_{1/2\ \text{light}}$. The flux was binned within each annulus whose radii grew with each pixel. Each annuli covered large distances of $0.2''$, or

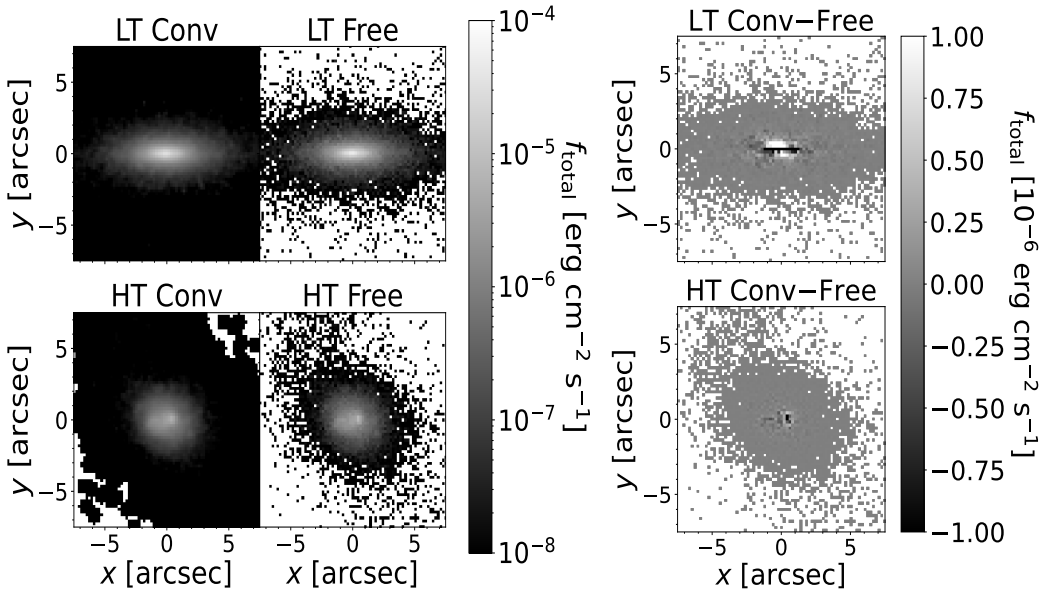

Figure 2.3: The IFU cubes were collapsed along the entire MUSE wavelength range. The collapsed images for a matched galaxy at both LT (top) and HT (bottom) runs are shown as Free, (left column) and PSF-convolved (middle column). The PSF is added by convolving a gaussian kernel with a FWHM of 0.3″. The residuals of Conv − Free are shown by the columns on the right. Both galaxies were placed edge-on, however, the HT galaxy does not have a clear disk, therefore it appears more elliptical.

approximately 0.67 kpc, and therefore, created discrete values at which $R_{1/2\ \rm light}$ could lie. This width was used as the error in the measurement of $R_{1/2\ \rm light}$. In order to avoid these large jumps, the flux was smoothed by extrapolating the assumed flux at intervals of 0.05 kpc. The relationship between $f_{\rm total}$ with respect to R is shown in Fig. 2.4 (left) for LT10213 both Conv (blue solid line) and Free (grey solid line). Also shown is the $R_{1/2\ \rm light}$ for the Conv galaxy as the dashed black line, and for the Free galaxy as the dot-dashed black line. The difference between the two half-light radii is minimal, approximately 0.10 kpc, but as the flux grows with R, the total Free flux deviates and becomes larger than Conv. We also explored the relation of the total flux with respect to the radius for a HT galaxy, shown in Fig. 2.4 (right). This galaxy is HT10712, the EAGLE HT match of LT10213. The Conv curve (red solid line) and its Free counterpart (grey solid line) display very little difference between the two, and the $R_{1/2\ \rm light}$ is nearly identical for both Conv and Free. We delve into the difference between LT and HT further on.

One way to compare the input EAGLE data and SimSpin's output was through the half-mass radius ($R_{1/2\ \rm mass}$) of the input data. Using the input EAGLE data, we calculated the radial distance of each particle from the centre of the galaxy (i.e. the centre of mass) using the particle's coordinates and binned them into

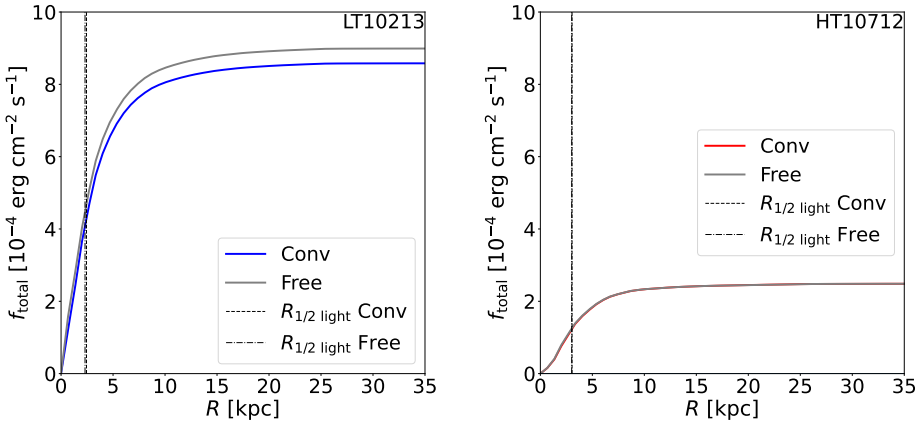

Figure 2.4: Total flux over R for a galaxy at LT and its HT match. *Left:* LT10213 flux Conv (blue line) and Free (grey line). The process of PSF convolution is removing part of the total flux from the galaxy early on, which reduces the overall flux. *Right:* HT10712 flux Conv (red line) and Free (grey line). Both Conv and Free follow a similar trend, meaning, unlike LT10213, the convolution process is not reducing the total flux, possibly as a result of the flux distribution in these galaxies, where LT has a bright bulge and thin disk while HT's flux is spread out over a larger area.

annuli the same size as the intervals of the extrapolated $R_{1/2\ \mathrm{light}}$, i.e. 0.05 kpc. Then we added the mass of every stellar particle within an annulus over the entire aperture, up to the outermost particle. The radius that contained the half mass was found by halving the total mass and finding the radius which contained this mass. Additionally, we added an intermediate step to draw direct comparisons between the half-mass radius and the half-light radius, in which the half-light radius at the particle level was determined. This involved generating an SED from the age and metallicity of each stellar particle and integrating over this function to find the luminosity of each particle. The SEDs were generated by interpolating the ages and metallicites with the EMILES template, as SimSpin does, and filtering the luminosity to the r-band. Once the luminsity of each stellar particle was calculated, the half-light radius at the particle level, $R_{1/2\ \mathrm{light\ part.}}$, was calculated in a similar way as $R_{1/2\ \mathrm{mass}}$: we sorted the particles into spherical annuli, added the luminosity of all the stellar particles, and found the half-light radius.

By comparing both $R_{1/2\ \mathrm{light\ part.}}$ vs $R_{1/2\ \mathrm{light}}$ and $R_{1/2\ \mathrm{light\ part.}}$ vs $R_{1/2\ \mathrm{mass}}$, as seen in Fig. 2.5 (top and bottom, respectively), we determined the difference between the mock galaxies and the input data. The data is shown for both LT and HT galaxies (blue circles and red squares, respectively), and the process of Conv (blue circles and red squares) and Free (grey diamonds) was compared in the bottom two plots to understand SimSpin's bias when processing the PSF convolution. The

uncertainties come from the annuli width (top panels) and the pixel width (bottom panels). The line of fits for all relationships, with the respective colours and the slope-intercept equations, are shown in the legend. The one-to-one relationship between these radii is shown by the solid black line; this linear relationship would be expected if the mass-to-light ratio of the galaxy was one. A trend of overestimation of the half-light radius with respect to the half-mass radius has been seen before in mock observations of simulations by Price et al. (2017) and de Graaff et al. (2022), where they found that overestimation is expected due to uncertainties from the mass-to-light ratios retrieved from SED fitting, and scatter is expected due to projection effects as a result of bright clumps that change according to the viewing angle. In that case, we could expect $R_{1/2\text{ light part.}}$ to overestimate $R_{1/2\text{ mass}}$ for both LT and HT since here is where the SED fitting is taking place. Regardless of the mass-to-particle-light distribution, we would also expect $R_{1/2\text{ light part.}}$ and $R_{1/2\text{ light}}$ to have a 1-1 relationship assuming the observational methods within SimSpin are not adding bias to the mock data cube.

From the top left plot we find that, for LT galaxies, the half particle-light radius is larger than the half mass radius, which reveals that star formation happens primarily at radii more extended than the stellar radius. This implies that, although there is more stellar mass concentrated in the centre, the brightest stars, those which were recently formed, lie further from the centre and therefore extend the half-light radius. When comparing this plot with the bottom left plot, showing LT's half particle-light to half-light radius, we can see that the process of mock observing is not adding any intrinsic bias to the observation and rather the line of fit for both Conv and Free lies close to the 1-1 line.

This, however, is not the case for HT. For HT galaxies, two outliers with $R_{1/2\text{ mass}} > 6$ kpc were removed from the sample since they were going through mergers and therefore, were guiding the slope of the line of fit towards a larger value. At HT, the half particle-light radius has nearly a 1-1 relation with the half-mass radius, showing that stellar mass and stellar light are equally distributed. This could either imply that star formation occurs throughout the galaxies with no clear bias towards inner or outer parts, or that the stars are older in age and hence the galaxies follow a similar mass-to-light trend with radius. Either way, we would also expect a 1-1 relation between the half particle-light radius and the half-light radius assuming SimSpin is not adding any bias; however, the bottom-right hand plot shows that the half-light radius at the particle level is increasing proportionally more than the half-light radius post-SimSpin for both Conv and Free, which follow a similar trend in their lines of fit. This trend differs from LT in the gradient; HT has a shallower gradient than LT. This implies that SimSpin is causing the decreasing

trend of the half-light radius by reducing the concentration of light close to the centre. We would expect to see this behaviour in both LT and HT unless HT is intrinsically different than LT. Understanding the exact source of this bias requires further analysis into the role of SimSpin in creating the data cubes, given that it could be due to a number of parameters. Since flux loss should not impact the derived kinematics of a galaxy, this lies beyond the scope of this thesis. However, the source of the difference in the slope of $R_{1/2\text{ light part.}}$ vs $R_{1/2\text{ mass}}$ was explored for LT vs HT galaxies.

In order to understand how the mass and the light are distributed within the sample of galaxies, we looked at the stellar age distribution of all the galaxies. The age of all stellar particles within the two threshold runs were binned and added as shown in 2.6, where LT galaxies are in blue and HT in red. LT galaxies have a peak in star formation at a lookback time between $4-3$ Gyr and it declines at higher redshifts. HT galaxies seem to have an earlier peak in star formation as the galaxy begins to form between a lookback time of $8-7$ Gyr, which declines slowly towards present age. The histogram shows that LT galaxies still have ongoing star formation events, shown by the bar close to 0 Gyr, which would explain the mass and light distribution explained previously. Additionally, it could explain why at HT, $R_{1/2\text{ light part.}}$ and $R_{1/2\text{ mass}}$ have a linear relationship, since a large number of stars in these galaxies are old. The differences between these two samples of galaxies can be attributed to the star formation gas density threshold, which has changed the structure, age distribution, and stellar distribution within these galaxies.

We explored the behaviour between Free and Conv for both LT and HT galaxies, as shown in the bottom two plots of 2.5, which shows that there is not a large difference added by the convolution, except that Free is systematically below its Conv counterpart. The difference between Conv and Free can be explained by looking at Fig. 2.4 (left), where Free has a steeper rise to its maximum flux, which reduces $R_{1/2\text{ light}}$. This behaviour is also seen in other LT galaxies and, as a result of the steeper slope, $R_{1/2\text{ light}}$ is smaller for Free galaxies. From Fig. 2.4, we can see that the HT galaxy's maximum flux is $\sim 1/3$ of the maximum LT flux and therefore has a shallower slope up to the point where the flux flattens out. A similar behaviour is seen in LT Conv vs Free, where LT Free has a steeper rise than Conv and, therefore, a smaller half-light radius. The same discrepancy between Conv and Free is not observed in the flux of HT10712.

From the plots of Fig. 2.5, we can see that Free is systematically below its Conv counterpart at LT and HT, showing that there is a systematic difference between processing a galaxy with and without PSF convolving, potentially due to the differences seen in the total flux. Fig. 2.7 shows the ratio of the total flux included

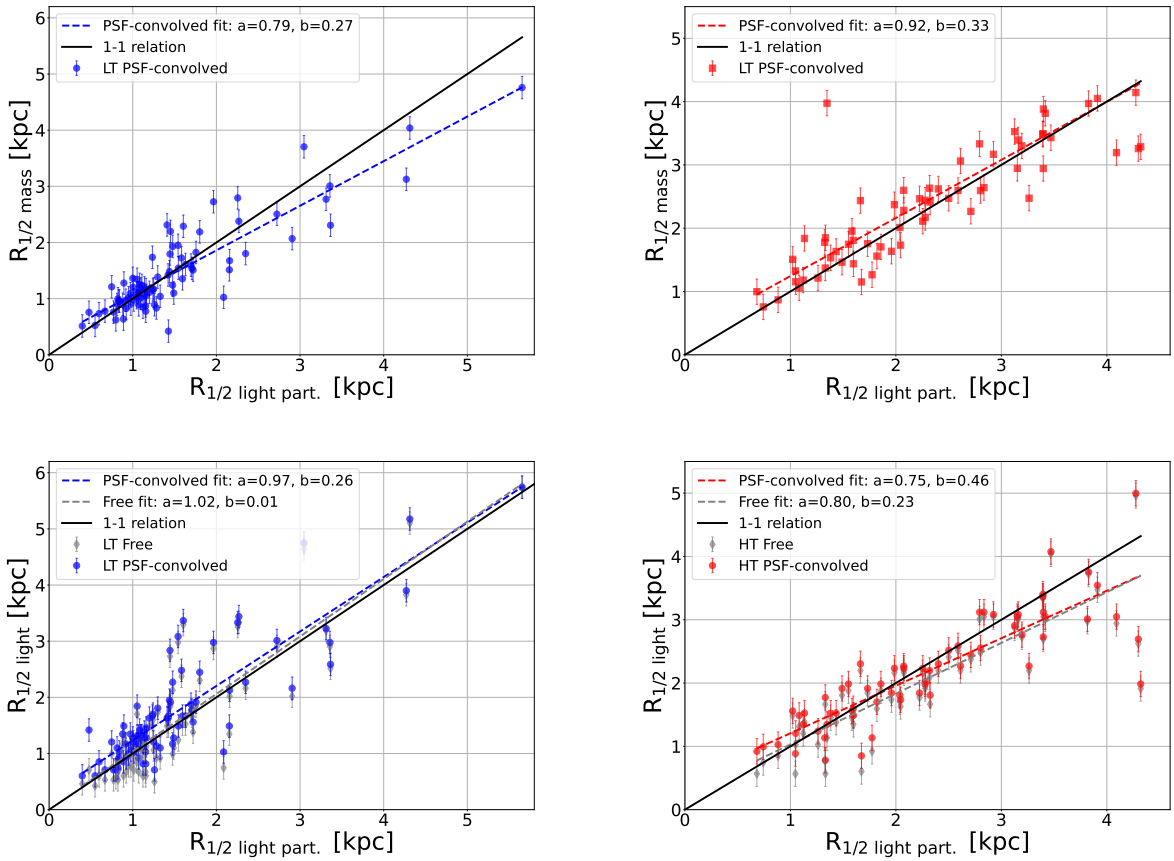

Figure 2.5: *Top:* $R_{1/2\ \text{light part.}}$ vs $R_{1/2\ \text{mass}}$ for LT (left) and HT (right) galaxies. The black line shown the 1-1 relation and the line of fit is plotted in the corresponding colour following the slope intercept ax+b. The error comes from the annuli width of 0.05 kpc. LT galaxies are systematically below the 1-1 line, meaning $R_{1/2\ \text{light}}$ is overestimating the $R_{1/2\ \text{mass}}$, unlike HT galaxies, which follow a 1-1 trend. *Bottom:* $R_{1/2\ \text{light part.}}$ vs $R_{1/2\ \text{light}}$ for LT (left) and HT (right) galaxies. Conv is shown as blue circles and red squares, while Free is shown as grey diamonds. The error comes from the pixel width of 0.2″. The one-to-one relationship is plotted as a black solid line and their lines of fit are plotted in the respective colours. LT galaxies follow a 1-1 trend while HT have a shallower gradient, where the half-light radii are underestimated at larger half-particle-light radii. In both HT and LT, Free galaxies have a $R_{1/2\ \text{light}}$ below their Conv counterpart.

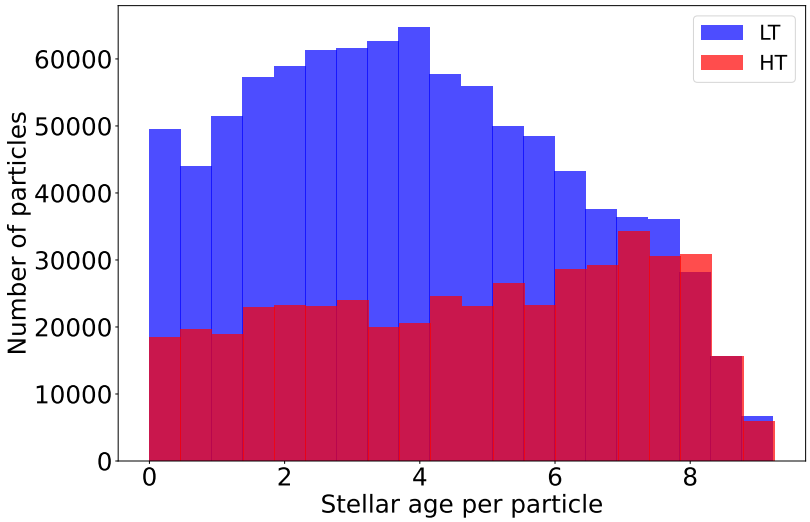

Figure 2.6: Stellar particle ages from EAGLE binned according to the distribution within LT (blue) and HT (red) galaxies. HT stellar ages peak around 7 Gyr and LT peak around 4 Gyr.

within the $15'' \times 15''$ aperture for Free galaxies, f_{Free}, with respect to the same galaxies Conv, f_{Conv}, and plotting it as

$$\frac{f_{\text{Free}} - f_{\text{Conv}}}{f_{\text{Conv}}}. \tag{2.2}$$

for both LT (left) and HT (right) galaxies. The reference line at 0 is plotted in black to show when both fluxes are equal. The galaxies' stellar mass was plotted since larger mass galaxies usually have a larger radial extent, meaning that by convolving it with a PSF, part of the total flux could have been smoothed over into pixels outside the aperture, therefore reducing the total flux. This upwards trend is seen in the LT plot, except for the four outliers which lie on the line where the flux is equal. These outliers have stellar masses close to the maximum cut-off point of the sample and three of them are going through a merger event. One difference can be observed between LT and HT galaxies, where the flux ratio of HT galaxies oscillates around the black line and the maximum value reached is ~ 0.0004 (or 0.04% of the total smoothed flux) without including the two outliers, which have a ratio beyond 0.001. In contrast, LT galaxies remain above the black line and the maximum value reached is ~ 0.05 (or 5% of the total smoothed flux), except for the four outliers.

The difference between LT and HT could be partly explained by the larger light concentration of the galaxies at LT vs HT, demonstrated by Fig. 2.8. The figure shows the relationship between $R_{1/2\ \text{light}}$ and the total stellar mass at LT (blue

circles) and HT (red squares), with the same errors as Fig. 2.5. Overall, HT galaxies have a larger $R_{1/2\ \mathrm{light}}$ than LT galaxies, meaning that most of the flux of LT is concentrated closer to the central bulge and thin disk, while HT have a larger spread of light distributed within the aperture. Additionally, we saw that the process of mock observing HT galaxies is adding a bias to the total luminosity and therefore reducing the half-light radius more than the particle half-light radius. Nevertheless, we still see that LT is more concentrated than HT galaxies, meaning the HT particle half-light radius would be expected to be even larger than the LT sample. However, we also saw the difference between a galaxy at LT and its HT counterparts in the residual plot of Fig. 2.5, where LT10213's peak in the residuals is concentrated in the bulge and thin disk. Meanwhile, HT10712 has smaller residual peaks smoothed over the centre. Since LT galaxies usually have a central bulge with a high luminosity peak in the centre, often one pixel wide, SimSpin is reducing the flux in the process of convolution, while HT galaxies have a smaller, more dispersed flux, which the convolution preserves. This reduction of the peak flux as a result of convolution is also seen in Chung et al. (2021). For larger, more luminous galaxies, the underestimation of the total flux could lead to problems when using light-weighted parameters. This process would also lead to variation concerning the structure and history of the galaxy, as we saw for LT and HT galaxies and their resulting half-light radii. However, for this study, a flux difference of 5% for LT galaxies should not produce large errors in the rest of this analysis. Further study would be necessary to understand the extent of this difference, such as fitting the full galaxies within the aperture, changing the FWHM of the PSF, and changing the spatial sampling.

2.6 Measuring the kinematics

Once the mock observations were produced for both the LT and HT galaxies Conv and Free, the next stage involved creating the kinematic maps. We use the GIST pipeline (Galaxy IFU Spectroscopy Tool, Bittner et al., 2019) to do so. GIST is a tool which reads IFU data and applies routines such as the penalised pixel-fitting (pPXF) method (Cappellari & Emsellem, 2004; Cappellari, 2017) and the Gas and Absorption Line Fitting (GandALF) software (Sarzi et al., 2006; Falcón-Barroso et al., 2006) to rapidly produce data usable for scientific analysis. GIST has been tested on galaxies at low and high redshift using data from MUSE and it has been used by the TIMER and PHANGS collaborations (Gadotti et al., 2019; Leroy et al., 2016). Both pPXF and GandALF are widely used routines used to extract the stellar kinematics and star formation histories, and the gaseous kinematics and

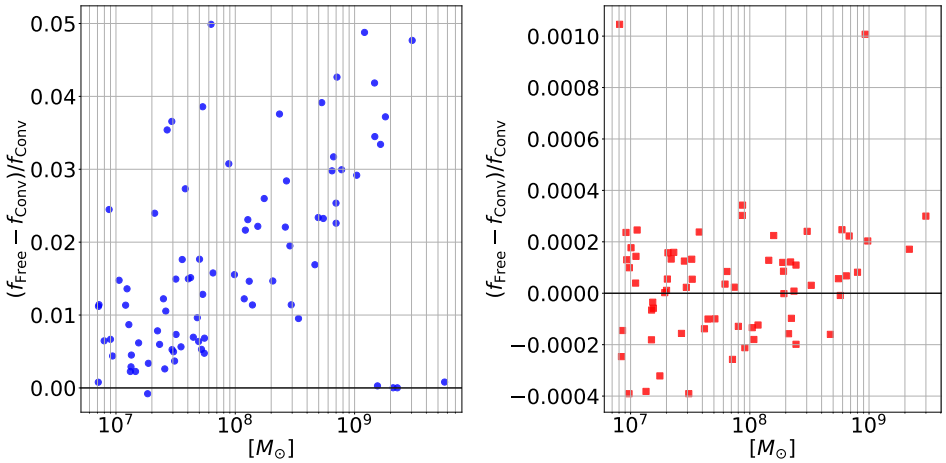

Figure 2.7: Flux difference between Free and Conv, normalised by the total flux at Conv (given by Eq. 2.2), with respect to the total stellar mass of the galaxy. When f_{total} Free and f_{total} Conv are equal, they should lie around the zero line shown by the black solid line. *Left:* LT galaxies lie consistently above the black line except for the four outliers at the higher mass end, which resemble HT galaxies in structure. There is an upwards trend, particularly pronounced for LT galaxies, which grows with stellar mass due to the flux lost outside the aperture in the smoothing process. *Right:* HT galaxies oscillate around the zero line with a difference in fluxes $\sim$ 100 times smaller than LT.

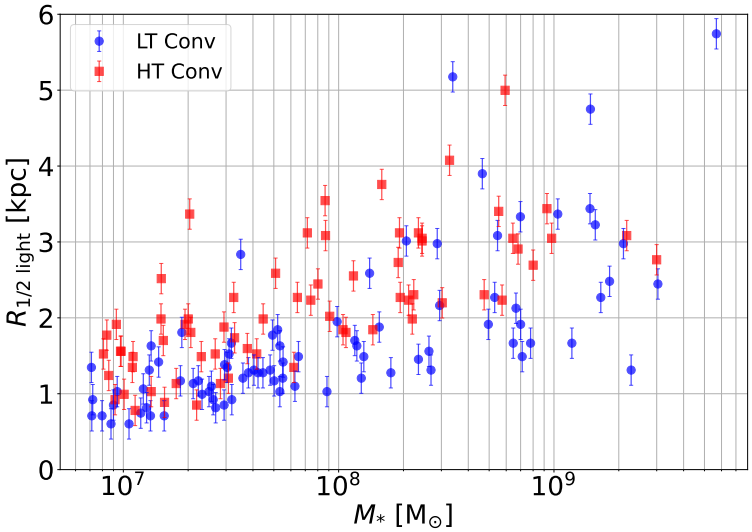

Figure 2.8: $R_{1/2\ \text{light}}$ with respect to the stellar mass of both LT (blue circles) and HT (red squares) galaxies. HT galaxies have a higher half-light radius than LT since their flux is less concentrated.

emission-line fluxes, respectively. We are interested in the role of pPXF rather than GandALF since we are only dealing with the stellar component of galaxies. pPXF recovers the line-of-sight velocity distribution (LOSVD) of the stars in a galaxy by deconvolving the spectra of a region in the sky with stellar population templates. These templates are produced using a sample of thousands of spectra taken with a spectrograph at a large range of atmospheric conditions and wavelength ranges. The line-spread function (LSF) of the templates is then convolved with a kernel so the template spectra match that of the observation. pPXF then simultaneously fits the LOSVD parameters such as the line-of-sight velocity, velocity dispersion, and the Gauss-Hermite parameters to find the ones that more closely reproduce the spectra and match the absorption lines, accounting for the redshift and the systemic velocity of the galaxy. Here we use EMILES as the stellar population template since we also used it previously to create the mock data. It has a spatial resolution of 2.51 Å. GIST convolves the spatial resolution of MUSE at each wavelength with its LSF to reproduce the LSF of the data.

To apply pPXF, GIST first reads in the data cube and shifts the spectra to the rest-frame wavelength based on the input redshift, then limits the wavelength range to the MUSE range (4700 - 9351 Å). This shifted data is applied the Voronoi binning method (Cappellari & Copin, 2003). This method adds up the signal of multiple spaxels until the signal-to-noise ratio reaches the target SNR. For this work, a target of 50 was chosen, and spaxels above this threshold remain unbinned. This value is widely used in literature since it maintains both the accuracy of the extracted data and the spatial resolution (van der Marel & Franx, 1993; Abril-Melgarejo et al., 2021). GIST calculates the noise in the data from the median flux at a given pixel, and assigns a normal distribution to the pixels. This is summarised by Equation 1 and 2 in Bittner et al. (2019). The binning routine also allows a minimum SNR to be selected, where spaxels below this limit will not be binned to avoid systematic effects at low surface brightness; a minimum ratio of 2.0 was chosen for this analysis (Flores et al., 2006). The SNR of the sample of galaxies processed exceeded the target for most spaxels near the centre of the galaxy. Single spaxel bins give a high effective spatial resolution in the inner regions.

GIST not only recovers information on the kinematic maps but also on the ages and metallicities of the stellar populations, which it extracts with pPXF by fitting the SSP library to the spectra and deducing the properties of the populations. An example of the line-of-sight velocity, age, and metallicity maps for galaxies LT10213 and HT10712 can be seen in Fig. 2.9, on the top and bottom row, respectively. Since both galaxies were built from the same initial conditions, the striking differences are due to the star formation gas density threshold's effect.

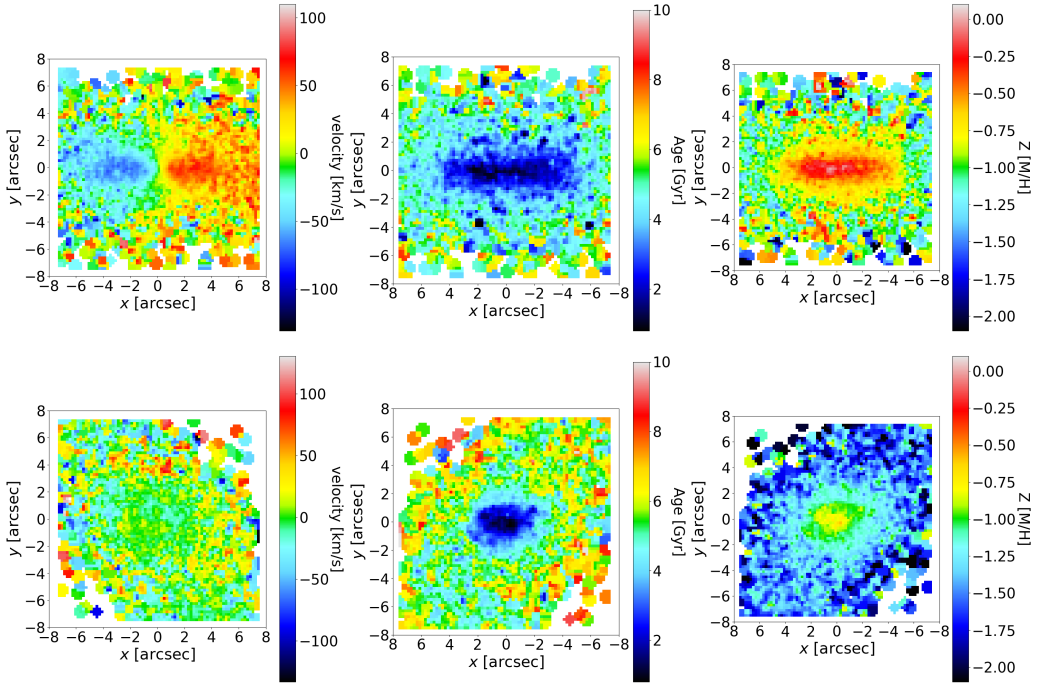

Figure 2.9: Output from GIST of the galaxies LT10213 (top) and HT10712 (bottom) of their LOSV map (left), ages (middle) and metallicities (right).

These galaxies have a stellar mass of 4.4×10^9 $M_\odot$ for LT and 4.3×10^8 $M_\odot$ for HT. The HT galaxy has fewer bins due to the smaller number of stellar particles and therefore, signal. Additionally, there is a clear difference seen throughout the three plots between the two runs, where the main one we care about is the velocity map since this was used to build the rotation curves. For LT10213, the rotation along a disk is clear, with the maximum and minimum values ranging from -100 km/s to 100 km/s. However, for HT10712, there is seemingly no rotation (in the stellar component at least), meaning the rotation curve can not be extracted through the method we used. Similar galaxies were removed from the analysis and we were left with 30 LT galaxies and 25 HT galaxies. These are some of the same galaxies Roper et al. (2022) selected for their analysis of the gas kinematics of mock observed galaxies from the same EAGLE runs, however, some of their sample was excluded due to a lack of a clear disk or unclear rotation axis. The same problems were not observed when looking at the stellar population data rather than the HI data. Once all the galaxies were processed through GIST, the rotation curves were extracted as described in the next chapter.

Chapter 3

Results

Once all the galaxies were analysed with GIST and the rotating galaxies were selected as described in Chap. 2, the major axis of rotation was determined. The major axis is the angle at which the disk of the galaxy is showing the maximal gradient in rotation velocity. Most of the galaxies were centred and placed along the major axis of rotation by SimSpin. However, some of the galaxies have a small number of stellar particles which, although gravitationally bound to the galaxy, are found at large distances and are disrupting the way SimSpin assumes where the centre and angle of rotation lie. This issue was resolved by ensuring that the rotating galaxies have a velocity close to zero at the dynamical centre of the galaxy, leaving an offset of approximately 2.8×10^{-4} kms^{-1}. Additionally, the kinematic major axis was determined by visual inspection since the distant particles have outlying velocities from the actual disk due to the scatter in the rotation further away from the centre, which was disrupting the automated method to determine this axis. An example of one galaxy which was individually shifted is LT13330, which was rotated by 20°of the original and the centre was shifted to the right. The velocity map for this galaxy is shown in Fig. 3.1. The bins further away from the bulk of the galaxy were causing the disruption.

3.1 Rotation curve extraction

Using the LOSV maps of the galaxies, the velocity of two rows of pixels along the disk of a galaxy, also known as a slit, was extracted from the GIST output. We calculated the mean of the two rows to form the rotation curve. A width of two pixels was chosen since it gives the best output rotation curve compared to a single slit or a slit of more pixels. The velocity map output from GIST for LT10213, a galaxy selected due to its clear rotation, is shown in Fig. 3.2 (top-left). An example

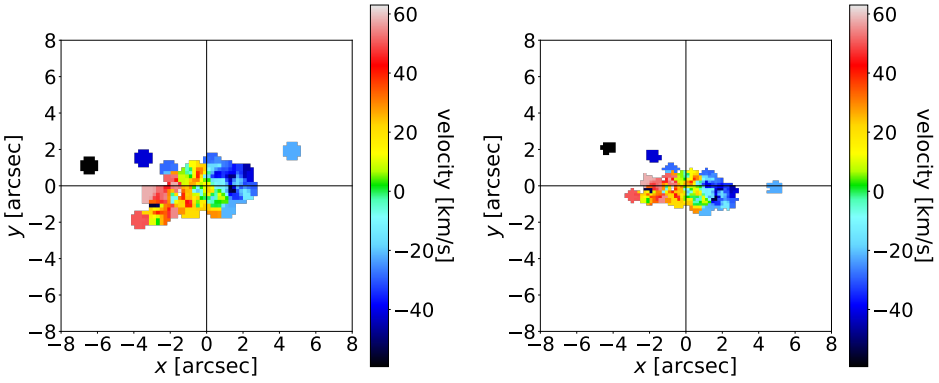

Figure 3.1: Velocity map of LT13330, a dwarf galaxy from the EAGLE sample, mock observed with SimSpin with added PSF. It was processed with GIST to create the velocity map. The Voronoi binning routine produced the three bins further from the bulk of the galaxy which are disrupting the centring of the galaxy and the rotation. *Left:* Original velocity map where the angle of rotation and centre is determined by SimSpin. *Right:* Same velocity map but shifted and rotated by visual inspection. The black vertical and horizontal lines show where the centre of the galaxy should be. The galaxy was rotated by 20 degrees and shifted to the right to fit into the centre.

of this slit is shown by the black horizontal lines, and the extracted rotation curve is given by the grey shaded area in the lower plot, V_{mock}, and its uncertainty. Hereafter, "rotation curve" refers to the line-of-sight velocity profile as a function of radius and is not corrected for asymmetric drift. Hence, we caution that it differs from the circular velocity profile, which translates directly to the enclosed mass. The uncertainty was determined by adding, in quadrature, the error in calculating the mean along with the error in the measured velocity produced by GIST for each bin. GIST's error map corresponds to the uncertainty of the fitting procedure of the SSP templates and the spectra. However, this contribution to the error is nearly negligible since, in principle, given that the star particles' spectra were produced using the same model spectra as used by the fitting routine, each pixel should have a perfect fit. Nevertheless, the error in each pixel still increases as the SNR becomes smaller, with the outskirts of the galaxies having higher uncertainties. Additionally, we performed a smoothing of the rotation curve by calculating the running median to achieve a clearer view of the rotation of the galaxy, which is given by the black solid line, labelled as V_{mock} smoothed.

We will be using multiple variables to define the velocities, labelled as:

- V_{circ}: Circular velocity (equivalent to the mass profile)

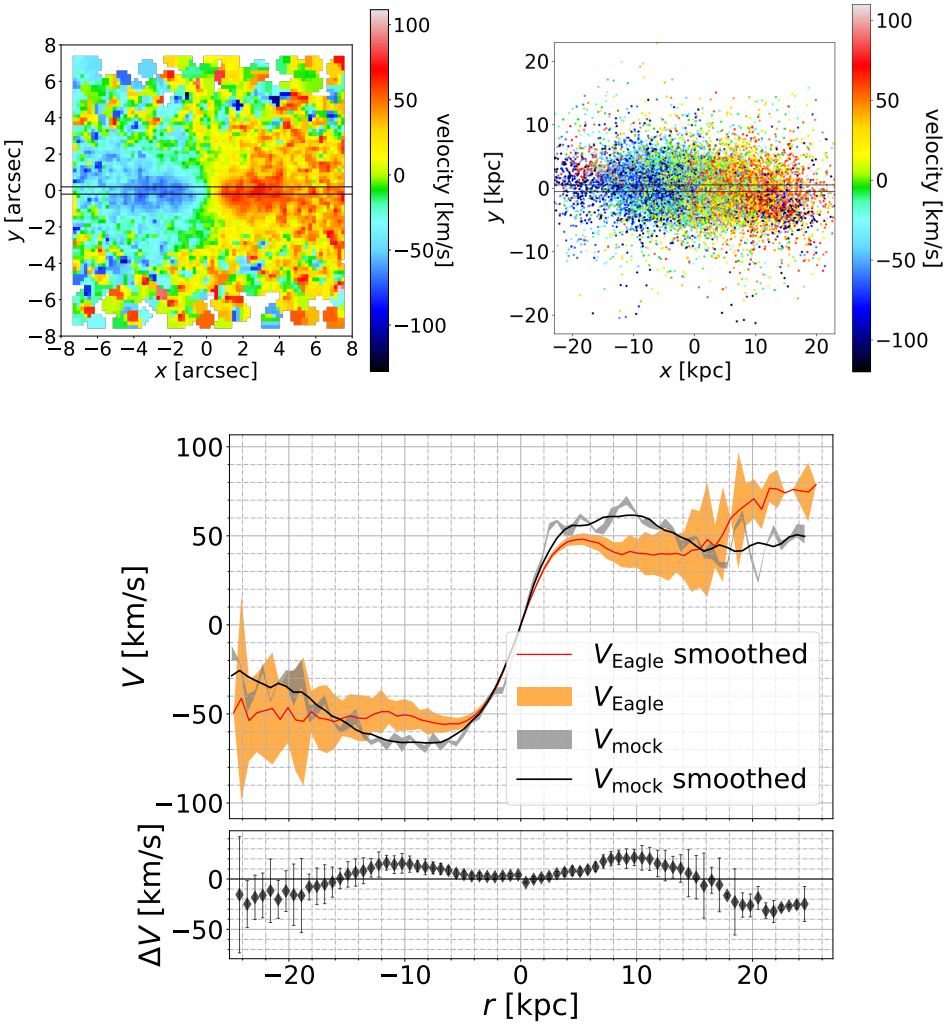

Figure 3.2: Galaxy LT10213's rotation curve and example of the slit. *Top-Left:* The LOS velocity map from GIST of this galaxy, along with the slit selected to extract the rotation curve (black horizontal solid lines), from which the mean of the two pixels (0.4") was used to form the slit to create the rotation curve. The galaxy is PSF convolved by SimSpin and then Voronoi binned by GIST. *Top-Right:* The LOS velocity map from the input EAGLE stellar particle data with the same slit width, which contains particles within a scale height of 0.67 kpc . The mean velocity was averaged in intervals of 0.67 kpc along the line of sight along the slit, imitating the procedure of GIST. *Bottom:* The rotation curves from the two slits are displayed here, where the grey shaded area plots the values from the mock observations and the smoothed data is shown by the black solid line (this is the running median). The orange shaded line shows the same rotation curve but from the plot on the right from EAGLE, and the red solid line is the smoothed version. The bottom panel shows ΔV as defined by Eq. 3.1. The errors come from the errors in the mock velocity and the EAGLE data velocity.

- $V_{\rm rot}$: LOS rotational velocity
- $V_{\rm EAGLE}$: Rotation velocity for the EAGLE un-mocked data
- $V_{\rm mock}$: Rotation velocity for mock data
- $V_{\rm max}$: Maximum velocity reached by $V_{\rm rot}$ from EAGLE ($V_{\rm max\ EAGLE}$) and from the mocks ($V_{\rm max\ mock}$)
- $V_{\rm fid}$: Velocity at the fiducial radius from EAGLE ($V_{\rm fid\ EAGLE}$) and from the mocks ($V_{\rm fid\ mock}$)

To draw comparisons between the mock observations and the simulations, we rotated and centred the input stellar particle data for each galaxy to match the viewing angle and centre created by SimSpin. We calculated the eigenvalues and eigenvectors of the inertia tensor of each galaxy to find the disk of rotation, set the rotation of the galaxy along the z-axis, and place the galaxy edge-on in the same way as SimSpin. The galaxies which had been previously individually rotated during the mock processing were rotated by the same angle and centred similarly by shifting the centre to the point where the LOSV is zero. The data was centred manually since particles further from the centre can disrupt the process of finding the centre and the plane of rotation, in the same way as in the mock observations. A slit containing particles within a scale height of 0.67 kpc, the same as the width of two pixels, was chosen to determine the rotation curve of the galaxies' input data. Additionally, the particle data was averaged in intervals of 0.67 kpc along the line of sight along the slit, imitating the procedure GIST would have done to produce the velocity maps once it collapsed the cube over each wavelength. This plot and the slit are shown in Fig. 3.2 (top-right) for the same galaxy (LT10213). Its LOSV as a function of the radius was plotted in Fig. 3.2 (bottom) for the region within 25 kpc ($7.5''$), shown by the shaded orange area, $V_{\rm EAGLE}$, which includes the error in this velocity given by the error in the mean. This rotation curve was smoothed in order to compare it with $V_{\rm mock}$, shown by the solid red line, $V_{\rm EAGLE}$ smoothed. The comparison between the input data, i.e EAGLE, and the mock rotation curves can be quantified by

$$\Delta V = |V_{\rm mock}| - |V_{\rm EAGLE}|, \tag{3.1}$$

which is shown in the bottom plot of the bottom figure. We see a clear difference between $V_{\rm mock}$ and $V_{\rm EAGLE}$. The errors come from the errors in $V_{\rm mock}$ and $V_{\rm EAGLE}$. Within the inner 14 kpc, mock observations overestimate the LOSV of the galaxy. This difference is specifically pronounced once the rotation curve begins to flatten, which occurs at ~ 4 kpc. It is possible that this difference is driven by the fact that we are looking at absolute ΔV rather than $\Delta V/V$. In the outer regions, the rotation

curve has associated large errors as a result of low SNR and few stellar particles. From this, we can draw the preliminary conclusion that mock observations do not reproduce the rotation curve from the input galaxy data, and they overestimate the expected velocities in the inner regions where the slope is flatter. This will be discussed in more detail in the following section, where we look at the role of PSF convolving in the rotation curves.

3.2 PSF Convolution comparison

PSF convolution could be affecting the shape of the galaxies' rotation curves, similar to how the peak flux was reduced by the beam-smearing effect. The same plot of the LOSV as a function of the radius is shown in Fig. 3.3 for LT10213 but the mock observation without any PSF, i.e, Free. This galaxy was created in the same way as the convolved version, except for the FWHM of the smoothing kernel which is set to zero. Additionally, GIST has the same fitting parameters and SNR as Conv, which resulted in the velocity map shown on the left and the rotation curve plot on the right. The main difference between Fig. 3.2 (bottom) and Fig. 3.3 (right) lies in the scatter of $V_{\rm mock}$, the grey shaded line, which is larger for Free. However, the extracted rotation curve itself is smoothed with the rolling median, as described above, resulting in the solid black line, which is qualitatively similar to the Conv rotation curve. In the original non-smoothed velocity curve, there is more noise in the velocity values across individual pixels. From the residual plot of the right Fig. 3.3, we can see that, on average, $\Delta V > 0$, meaning the Free mock observation is also overestimating the LOSV of the galaxy.

This pattern is also seen in some other rotating galaxies as seen in Appendix A.1 for both LT and HT galaxies; however, the main characteristics observed are the differences from one galaxy to the other. To study the trends, we looked at the velocity difference within a radial distance from the central 2 kpc of each galaxy, where there is less scatter in the non-smoothed rotation curves. In Fig. 3.4, we plotted $(|V_{\rm mock}| - |V_{\rm EAGLE}|)/V_{\rm mock}$ for both Conv (left) and Free (right) mock observations of LT and HT rotating galaxies. Fig. 3.4 shows the normalised ΔV for the LT and HT as a whole, respectively, in the form of violin plots. The width of each violin indicates the frequency of a given $\Delta V/V_{\rm mock}$ value across all galaxies. The vertical bars and whiskers in the centre show the interquartile range and the median as the white point. $\Delta V/V_{\rm mock}$ is consistent with 0 at the 50% confidence interval for both Conv and Free at HT and LT. However, the median of the normalised ΔV for HT galaxies lies above the zero line by $8\pm30\%$ for Conv, and Free by $25 \pm 35\%$, meaning that the mock rotation curves could be systematically

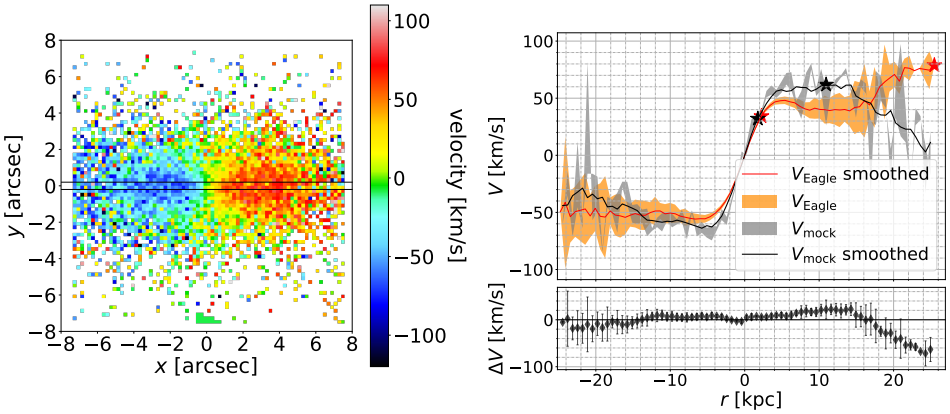

Figure 3.3: Velocity map and rotation curves for LT10213 without PSF convolution. *Left*: Velocity map output from GIST of the galaxy without added PSF and the slit chosen to form the rotation curve, shown in black. *Right:* Rotation curve given by the LOSV with respect to the radius of the galaxy. The rotation curve from the mock observation is shown as the grey-shaded area with the error in the mean, and the smoothed curve is shown as the black solid line. The rotation curve from the input EAGLE data is shown as the orange shaded area, with the smoothed curve as the red solid line. The residuals between the two lines, ΔV, are displayed at the bottom of the figure, where most of the central points lie above the zero line, similar to the plot of LT10213 Conv in Fig. 3.2

overestimating the EAGLE rotation curves at the HT. One difference lies in the shapes of LT vs HT, where LT galaxies are concentrated closer to $\Delta V \approx 0$ kms^{-1}, while HT is spread wider around the median, meaning that there is more scatter in the HT than in the LT.

One likely reason is the difference in structure between LT and HT, where HT galaxies tend to be more spheroidal and hence have less rotation along a disk. The rotation of the stellar particles was quantified by determining the fraction of kinetic energy each galaxy has invested in ordered rotation, using the equation from Correa et al. (2017),

$$\kappa_{\rm co} = \frac{K_{\rm rot}}{K} = \frac{1}{K} \sum_{i}^{r<30{\rm kpc}} (\frac{1}{2} m_i [\frac{L_{z,i}}{(m_i R_i)}]^2, \tag{3.2}$$

where we sum the kinetic energy over all stellar particles within a spherical radius of 30 kpc. K is the total kinetic energy

$$K = \sum_{i}^{r<30{\rm kpc}} (\frac{1}{2} m_i v_i^2), \tag{3.3}$$

m_i is the mass of each stellar particle, v_i is the total velocity of each particle, $L_{z,i}$ is the particle's z-component of the angular momentum, where the z-axis coincides

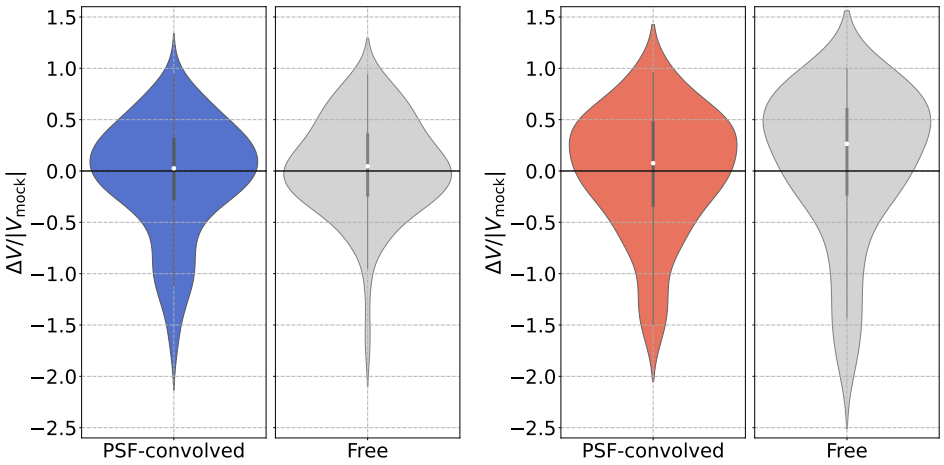

Figure 3.4: Violin plots of the normalised $(|V_{\rm mock}|-|V_{\rm EAGLE}|)/V_{\rm mock}$ for the inner 2 kpcs of each selected rotating galaxy of the sample. *Left:* LT Conv is shown in blue and LT Free is shown in grey. The width of the violin plots shows the distribution of values, which are overplotted by the vertical bars and whiskers showing the interquartile range as the thick black line, the 95% confidence interval as the thin black line, and the median as the white point. *Right:* HT Conv is shown in red and HT Free is shown in grey. The same description for the quartiles applies. All four violin plots lie at 0 at a 50% confidence level, meaning there is no systematic overestimation. However, there is a large scatter in the range of values, meaning that the mocks are not replicating the behaviour of $V_{\rm EAGLE}$ accurately.

with the angular momentum vector of the galaxy, and R_i is the distance to the axis of rotation of the galaxy. The galaxies with $\kappa_{\rm co} < 0.4$ are defined as ellipticals and galaxies with $\kappa_{\rm co} > 0.4$ as discs. For this sample of rotating galaxies, $\kappa_{\rm co}$ was calculated, where the median value of LT is 0.39 ± 0.02 and HT is 0.35 ± 0.02. Some LT galaxies have a corotation value above 0.4 while HT galaxies tend to stay below 0.4. This reveals HT galaxies tend to be more spheroidal in shape, leading to a larger scatter in ΔV. As a result, HT galaxies have rotation curves which deviate from the input velocities by a larger value than LT. The difference seen between HT Conv and Free is also a source of concern since it is not prevalent between LT Conv and Free. This distinction could be due to the scatter found in the non-convolved rotation curves, which deviate from the smoothed velocities and, therefore, lead to larger uncertainties in the data.

3.3 Changes to LT10213

Overall, since the galaxies are centred on $\Delta V \gtrsim 0\ {\rm kms}^{-1}$, the process of making the mock observations is seemingly overestimating the rotation curves from EAGLE, particularly for HT. However, there is still a large scatter in the differences between

$V_{\rm mock}$ and $V_{\rm EAGLE}$, which means that individual galaxies are deviating from the EAGLE rotation curve both towards positive and negative ΔV's. One example is LT10213, which deviates from $V_{\rm EAGLE}$ as both Free and Conv. LT10213 has a large total flux and clear rotation along its disk, without disruptions by star formation events, meaning that the differences caused by the spectral fits are minimised, therefore, it allowed us to explore other sources of uncertainty. To investigate the differences in the rotation curves, different versions of the mock for this galaxy were produced: e.g. by reducing the SNR target on GIST from 50 to 5, and using the Bruzual & Charlot (2003) SSP template rather than EMILES. This template was only used to make the mock IFU cube with SimSpin, however, it was processed with GIST using EMILES to ensure consistency in the post-processing methods. The effect of these changes is shown in Fig. 3.5 for LT10213. The plot on the left shows violins, where the median ΔV is larger than zero for the region within the central 2 kpc of the first three violins, where $V_{\rm mock}$ Conv is shown in green, Free in pink, low SNR in blue, and the Bruzual and Charlot (BCl henceforth) template in purple. The right panel of Fig. 3.5 shows the rotation curves resulting from the different mock runs, colour-coded in the same way as the left panel, including $V_{\rm EAGLE}$ which is shown in black. The PSF convolution is expected to result in a flatter slope of the rotation curves and therefore deviate more from $V_{\rm EAGLE}$ due to the smearing effect of the PSF as seen in Figure 12 of Kendrew et al. (2016). However, the difference between Conv and Free is not clear from Fig. 3.5 as a result of the small value of PSF FWHM used. Next, the effect of a decreased SNR target value in GIST was explored, which should resemble more closely the input data in the inner regions since here, we find single spaxel bins. However, we find that the slope of the resulting curve (blue line in Fig. 3.5) is steeper than Conv or Free. Additionally, the median ΔV increased, which reflects the data seen in the rotation curves for the region within 2 kpc. However, although the curve deviates in the inner regions and at $r < 0$ kpc, when $V_{\rm EAGLE}$ flattens out at $r > 0$ kpc, the low SNR seems to match it more closely.

Also shown is the effect of changing the template to BCl: ΔV's range increased, meaning there is a larger dispersion between the mock and the input EAGLE rotation curves. By applying the BCl template, we show that the choice of template affects the LOSV, particularly when the same template is not used for the post-processing. Further tests are needed to quantify the differences caused by the use of an SSP template, in particular by comparing various templates and applying the same template both to SimSpin and GIST. Quantifying this is important to the development of mock observations since the use of different templates can affect the stellar age and metallicity distribution within a galaxy (Guidi et al., 2018), however, a comparison between these is beyond the scope of this dissertation.

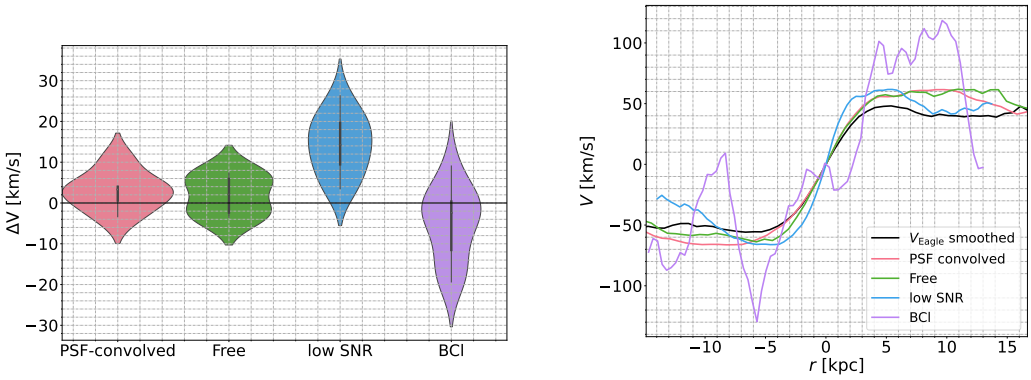

Figure 3.5: *Left:* Residual plot of ΔV for LT10213 showing different ways of mock observing the galaxy and their residuals within 2 kpc. Pink: Conv image with SNR of 50 with its median at 0 kms^{-1}; Green: Free image with SNR of 50 similar to Conv in its median but with larger spread both above and below 0 kms^{-1}; Blue: low SNR threshold of 5 on GIST and Conv through SimSpin; Purple: Applying Bruzual & Charlot (2003) to SimSpin Conv and SNR of 50. *Right:* Full rotation curves of the four different runs in their respective colours and V_{EAGLE} shown in black. There is a deviation seen on all curves, which varies depending on the parameter chosen and the region observed.

3.4 Inner and outer rotation curves

In theory, by reducing the SNR and not performing the PSF convolution, the rotation curves extracted from the mock cubes should resemble those extracted from the EAGLE data directly. However, as shown in the previous section, one (or more) of the steps in the process of creating the mock cubes lead to a discrepancy between the mocks and the unprocessed EAGLE data (see e.g. Fig. 3.5). This systematic discrepancy occurs through all the methods attempted, which tells us that we still do not know where it is coming from. We can determine the significance of the differences between the mock and un-mocked rotation curves by comparing a specific relationship, such as the ratio between the inner and outer velocities.

In order to study SimSpin's and GIST's ability to recover the EAGLE un-mocked rotation curves at different radii, we looked at the point of maximum velocity, V_{max}, and the fiducial velocity, V_{fid}, which is the rotational velocity at the point where the fiducial radius,

$$R_{\mathrm{fid}}/\mathrm{kpc} = V_{\mathrm{max}}/35\mathrm{kms}^{-1}, \tag{3.4}$$

This method of looking at the inner rotation curve was defined in Equation 1 of Santos-Santos et al. (2020) where the value of V_{fid} adapts to the size of the galaxy and traces its dark matter content.

In their analysis of the atomic gas, Roper et al. (2022) found a difference between

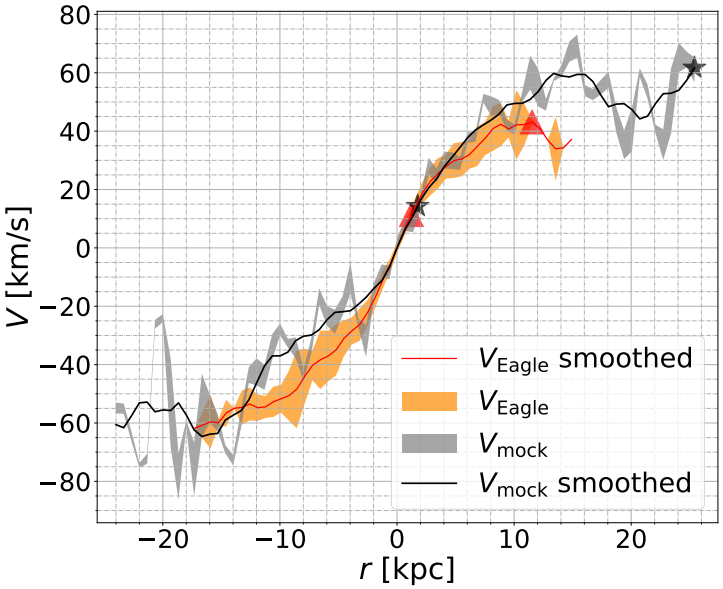

Figure 3.6: LT12300 Conv rotation curves from V_{EAGLE} in orange and V_{mock} in black. $V_{\mathrm{fid\ mock}}$ and $V_{\mathrm{max\ mock}}$ are labelled on the graph as the black stars and $V_{\mathrm{fid\ EAGLE}}$ and $V_{\mathrm{max\ EAGLE}}$ are shown by the red triangles. V_{max} extends out further than V_{fid}. The radial extent of this galaxy is seemingly larger for V_{mock} as a result of the binning routine, which is taking discrete particles and assigning a velocity to a region which is not included within the slit of the EAGLE velocity maps.

LT and HT galaxies in terms of V_{fid} and V_{max} from the circular velocities. However, given that stellar particles do not reach as large radii as gas particles, the purpose of this study is to see where the differences between the mock observations and the EAGLE data lie and determine if we can observe a similar pattern to what Roper et al. (2022) found. We compared the values of V_{max} and V_{fid} for the rotation curves from the mock observations and the input EAGLE data to determine whether there is a clear difference seen for both LT and HT rotating galaxies when observed with PSF convolution. An example of one of these galaxies is shown in Fig. 3.6, where the rotation curve for LT12300 Conv is shown with V_{fid} and V_{max} indicated by the red triangles and black stars for the input EAGLE and the mock data, respectively.

Fig. 3.7 shows the ratios between $V_{\mathrm{max\ mock}}/V_{\mathrm{max\ EAGLE}}$ and $V_{\mathrm{fid\ mock}}/V_{\mathrm{fid\ EAGLE}}$ for all rotating galaxies for LT (circles) and HT (squares), which are coloured based on their κ_{co} value. The black lines indicate where the ratios are equal to one, meaning the mock velocities and EAGLE are equal. The difference between the left-hand plot and the right-hand plot lies in the values of R used to define the fiducial radius and the maximum radius. On the left, we show the mock and input EAGLE velocities at the fiducial and maximum radii from their respective mock and input radii, while on the right, we used the same fiducial and maximum radii

obtained from the input EAGLE data for both the mock and the EAGLE velocities. By using the same radii as EAGLE on the mocks, we can single out whether the error lies in the choice of radii or the rotation curves altogether. From the example in Fig. 3.6, we see that $R_{\rm max}$ differs between EAGLE and mock rotation curves, which, in turn, affects $V_{\rm max}$ and hence the fiducial radius and velocity.

The main difference between the two panels in Fig. 3.7 lies in the upper right-hand region, where both the maximum and the fiducial velocities of the mock data are larger than the maximum and fiducial velocities of the input EAGLE data. When $R_{\rm mock}$ is used to calculate the corresponding fiducial and maximum velocities from the mock rotation curves, most galaxies lie in the upper right-hand plane, where the velocities are overestimated by the mocks, in particular galaxies with $\kappa_{\rm co} < 0.4$, which are galaxies which are more spheroidal and have less ordered rotation along a disc. Galaxies with $\kappa_{\rm co} \geq 0.4$ lie in the bottom left quadrant, where mock velocities are underestimated, however they tend to stay closer to the 1-1 ratio. On the right-hand plot, where we use the radius of the fiducial and the maximum velocity from $R_{\rm EAGLE}$ and apply it to the mock rotation curves to obtain the velocity at those radii, neither mock nor EAGLE is consistently larger or smaller. The inner velocity of spheroidal galaxies is still being overestimated by the mock rotation curves and underestimated for disc galaxies, however, disc galaxies remain closer to the 1-1 ratio. The median of the ratio of $V_{\rm max\ mock}/V_{\rm max\ EAGLE}$ changes from ~ 1.33 to ~ 1.10, and the median of the ratio of $V_{\rm fid\ mock}/V_{\rm fid\ EAGLE}$ changes from ~ 1.44 to ~ 0.92. Therefore, when using the EAGLE radial values, the mock fiducial and maximum velocities match those from EAGLE more closely, particularly for disc galaxies. This is expected since there is less scatter in the rotation of disc galaxies, which means that there will be less dispersion between the calculation of the two velocities. Although we see this difference here, when making real observations, the expected radii are not known, which could explain why observations do not exactly match the velocity profiles of simulations, as explained in Chap. 1. We considered the effect of the number of particles on the accuracy of the results, however, since the number of particles changes only by a factor of 100, we did not find any relation.

The difference between using the mock radius vs the EAGLE radius was explored by looking at $R_{\rm fid}$ and $R_{\rm max}$, since the over or underestimation of the radius could explain the discrepancy between measured velocities. Fig. 3.8 shows the ratio of $R_{\rm max\ mock}/R_{\rm max\ EAGLE}$ and $R_{\rm fid\ mock}/R_{\rm fid\ EAGLE}$ for both LT and HT galaxies. The black lines show where the ratios equal one. The data points are coloured by stellar mass. Most of the data points lie where $R_{\rm fid\ mock} > R_{\rm fid\ EAGLE}$ and $R_{\rm max\ mock} > R_{\rm max\ EAGLE}$, similar to the left-hand plot of Fig. 3.7. Upon further inspection, it is apparent that the overestimation of $R_{\rm mock}$ (or the underestimation

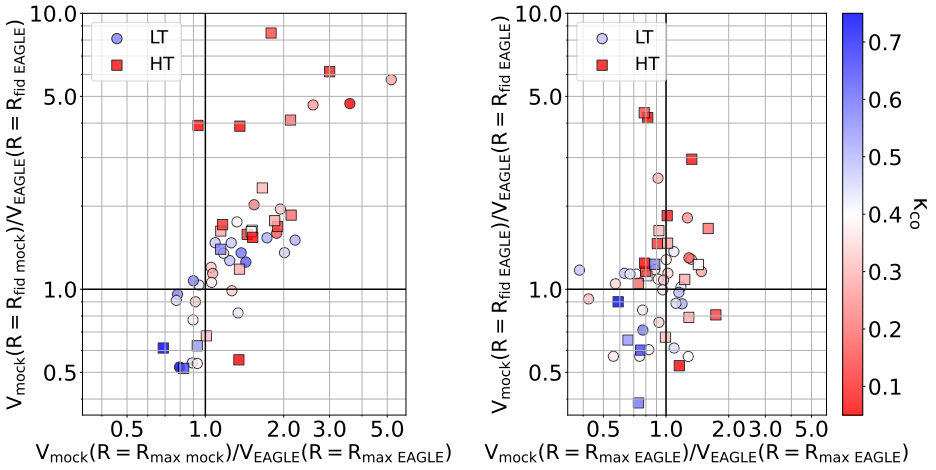

Figure 3.7: Ratios between $V_{\text{max mock}}/V_{\text{max EAGLE}}$ and $V_{\text{fid mock}}/V_{\text{fid EAGLE}}$ for all rotating galaxies for LT (circles) and HT (squares), which are coloured based on their κ_{co} value. We define galaxies with $\kappa_{\text{co}} < 0.4$ as spheroidals and galaxies with $\kappa_{\text{co}} \geq 0.4$ as discs. The black lines indicate where the ratios are equal to one. *Left:* The mock and input EAGLE velocities at the fiducial and maximum radii from their respective mock and input radii. *Right:* Used the same fiducial and maximum radii obtained from the input EAGLE data for both the mock and the EAGLE velocities. There is a variation between the two, particularly on the top right-hand quadrant, where the mock rotation curves overestimate EAGLE due to the chosen R values, particularly for spheroidal galaxies.

of R_{EAGLE}) is due to the EAGLE data not extending to the same large radii as the mock data. This was shown in Fig. 3.6, which shows the rotation curve of LT12300. This is a galaxy with a stellar mass of 3.4×10^8 $M_\odot$, over 4 times smaller in mass than LT10213 (whose rotation curves for mock and EAGLE extend equally as far) and therefore has a shorter radial extent. The difference in the mass and hence the radial extent could explain why V_{EAGLE} does not extend as far as V_{mock}, shown by the colours of Fig. 3.8. The more massive galaxies lie close to the (1,1) intersection, while less massive galaxies have some scatter towards the upper right-hand corner. This extent is a result of the binning procedure, where stellar particles from the input EAGLE data not included in the slit, are processed by SimSpin and then PSF convolved, which GIST then bins into larger bins until the minimum SNR threshold is reached. These bins often fall within the slit, resulting in more extended rotation curves from the mock data. Since higher mass galaxies have a larger radial extent with more particles out to the FOV of the aperture of the observation, they lie within the slit and extend the EAGLE rotation curve. In order to avoid this discrepancy from the difference in radial extent, a mask should be placed around the velocity maps, which removes the rogue pixels which

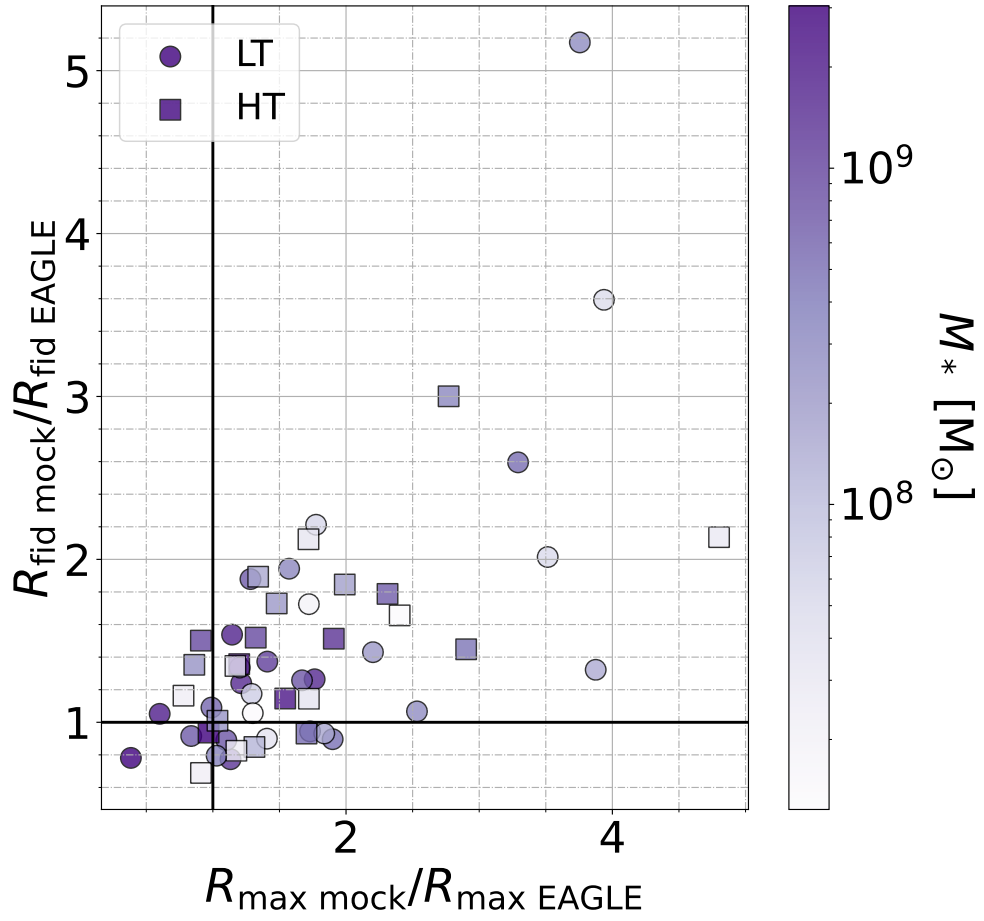

Figure 3.8: Ratio of $R_{\text{max mock}}/R_{\text{max EAGLE}}$ and $R_{\text{fid mock}}/R_{\text{fid EAGLE}}$ for both LT (circles) and HT (squares) galaxies. The black lines reveal where the ratios equal one. The data points are coloured by stellar mass. Most of the data points lie where $R_{\text{fid mock}} > R_{\text{fid EAGLE}}$ and $R_{\text{max mock}} > R_{\text{max EAGLE}}$, showing that the mock galaxies are overestimating the values of the radii. This occurs due to the longer extent of the rotation curves as a result of the Voronoi binning process. This effect is emphasized for lower-mass galaxies, which have a larger radial extent.

are separated from the bulk of the galaxy. Due to the difference in extent, often $R_{\text{max mock}}$ lies beyond the extent of R_{EAGLE}, which explains why the maximum radius from the mocks is larger than that from EAGLE in some cases. In other cases, such as LT10213, the curves have a different shape altogether, so R_{max} is reached at different points.

We also explored mock observations' ability to reproduce the relationship between V_{fid} and V_{max}, which was explored by Roper et al. (2022) for the circular velocity of

the atomic gas. However, in their analysis, they have corrected the rotation curves for pressure support, and therefore their results show larger velocities compared to this analysis for both LT and HT galaxies. The relationship between the inner and outer rotation curves (i.e. $V_{\rm fid}$ and $V_{\rm max}$), as explained in Chap. 1, can be an indication of the dark matter distribution within a galaxy. If mock observations can reproduce either the large scatter seen from observations or the clear relation from simulations, it could be evidence of the discrepancy between the two. We explore this for our mock observations in Fig. 3.9, both for LT and HT galaxies using: the maximum and fiducial radii from the mocks (left panel), the radii from EAGLE on the mock rotation curves (middle panel), and compare this with the values from the input EAGLE galaxies (right panel). The left-hand figure shows $V_{\rm mock}(R = R_{\rm fid\ mock})$ and $V_{\rm mock}(R = R_{\rm max\ mock})$. LT (blue circles) and HT (red squares) populate the figure and, in the same colours, the fit's intercept-slope for each threshold as the dashed lines, with the standard deviation in the shaded line. We use the black solid line as the expected relation for the cusped NFW profile as a point of comparison, assuming the mass-concentration relation of Ludlow et al. (2016) where $V_{\rm fid} \approx 0.65 V_{\rm max}$. However, any real comparison with this reference line should be done with the circular velocity rather than the rotation velocity. The middle plot shows $V_{\rm mock}(R = R_{\rm fid\ EAGLE})$ and $V_{\rm mock}(R = R_{\rm max\ EAGLE})$, meaning the R values selected from the simulated curves on the mock curves. The right plot shows $V_{\rm EAGLE}(R = R_{\rm fid\ EAGLE})$ and $V_{\rm EAGLE}(R = R_{\rm max\ EAGLE})$ as a point of comparison for the other two plots. One difference for LT lies in the short range of values of the maximum velocity from the mocks using the mock radii (left panel) compared to the maximum velocity from the EAGLE using the EAGLE radii (right panel), possibly as a result of the longer extent reached by $V_{\rm mock}$. This difference is compensated when using $R = R_{\rm max\ EAGLE}$, which reduces the scatter in the maximum velocities reached by the mock rotation curves. We do not see this same scatter in HT since the sample of HT is smaller than LT, which limits the range of velocities. By using $R = R_{\rm max\ EAGLE}$ on the mock data, we are relying on knowing the results from the simulations. However, in actual observations, the real parameters are not known, which makes this assumption unrealistic. This comparison was made to show that the way we processed these galaxies led to the overestimation of $V_{\rm max}$ for LT galaxies, deviating further from the EAGLE data.

The values from $V_{\rm EAGLE}$ have a tighter relation to the fits compared to the other two plots of $V_{\rm mock}$, which shows that there is a difficulty in replicating specific parameters from these mock observations. Here, we demonstrated how the process of making mock observations and analysing them increases the number of possible $V_{\rm fid}$ per $V_{\rm max}$; nevertheless, some galaxies manage to maintain similar values as those from EAGLE, as we saw in Fig. 3.7 and 3.8. However, the issue lies in the

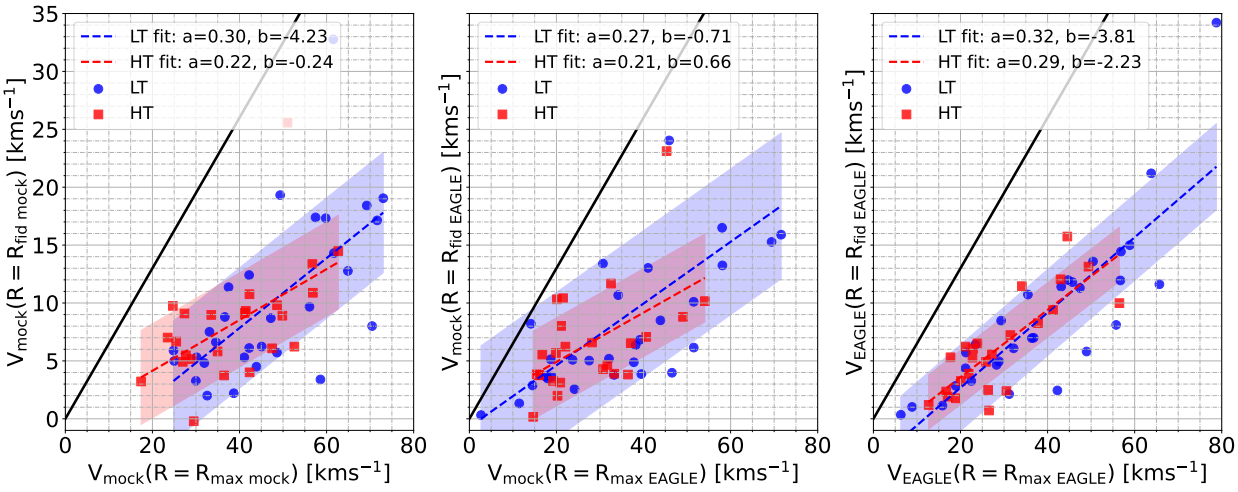

Figure 3.9: *Left:* $V_{\mathrm{mock}}(R = R_{\mathrm{fid\ mock}})$ and $V_{\mathrm{mock}}(R = R_{\mathrm{max\ mock}})$ for LT (blue circles) and HT (red squares). In the same colours, the fit's intercept slope for each threshold is shown by the dashed lines, with the standard deviation as the shaded line. We use the solid black line as the expected relation for the cusped NFW profile as a point of comparison, assuming the mass-concentration relation of Ludlow et al. (2016). *Middle:* $V_{\mathrm{mock}}(R = R_{\mathrm{fid\ EAGLE}})$ and $V_{\mathrm{mock}}(R = R_{\mathrm{max\ EAGLE}})$, meaning the R values selected from the simulated curves on the mock curves. *Right:* $V_{\mathrm{EAGLE}}(R = R_{\mathrm{fid\ EAGLE}})$ and $V_{\mathrm{EAGLE}}(R = R_{\mathrm{max\ EAGLE}})$ as a point of comparison for the other two plots.

populations as a whole, where we found discrepancies in the data. This scatter was also observed in Fig. 3.4, meaning that while some galaxies have rotation curves that match the input EAGLE data, others deviate by a significant amount. In particular, we found issues with HT galaxies, which have bursts of star formation which alter the fitting routines and therefore the rotation curves. Further analysis is needed to determine if the methods used to analyse observations lead to this difference, i.e. GIST and the rotation curve extraction method, or if the methods of making mock observations are the source of uncertainty, i.e SimSpin.

Chapter 4

Discussion

In this work, we exploited the capabilities of the SimSpin software (Harborne, 2019) to recover the kinematic properties of dwarf galaxies within EAGLE. To this end, we produced mock observations of a sample of 158 dwarf EAGLE (Schaye et al., 2015) galaxies using SimSpin with the parameters of the MUSE instrument (Bacon et al., 2010). We further exploited the impact of star formation recipes on the stellar kinematics of this population by post-processing two EAGLE runs with two star formation density thresholds. The ultimate goal of this work was to understand the impact of star formation activity on the dark matter distribution and evaluate the ways of retrieving this distribution. This has been explored through the differences in the rotation curves, particularly in the inner regions versus the outer regions, where simulated EAGLE galaxies created at a higher threshold developed a constant density core while lower threshold galaxies have a steeply rising cusp. This clear difference in behaviour has not been reproduced in observations of dwarf galaxies, since the dark matter distribution in the inner regions of a galaxy can vary greatly for different galaxies with the same stellar mass. Since simulations do not reproduce this scatter, we looked at mock observations to understand if the traditional methods used to analyse observations could be adding an unknown level of uncertainty or scatter. However, to reproduce this comparison, we first had to ensure the mock observations from SimSpin were reliable.

- The sample of galaxies was mock observed with two prescriptions for beam smearing: 1) with a PSF convolution at a FWHM of $0.3''$, and 2) without the convolution. Although SimSpin managed to maintain accuracy between the PSF convoluted and non-convoluted versions of a galaxy up to a 5% difference in the total flux, there were still discrepancies for LT galaxies at their peak

brightness. However, this same reduction was not observed in HT galaxies as a result of their structure, showing that different structures can lead to larger scatter in the observations. Chung et al. (2021) also saw differences in the peak flux reached by PSF-convolved IFU images since the flux at the peak gets smoothed. Since LT galaxies have a bright bulge and thin disk, the flux from the central pixels is reduced and dispersed though the convolution. HT galaxies have multiple peaks of brightness, which leads to a smaller change through the convolution. By reducing the flux of a galaxy, some parameters were overestimated, such as $R_{1/2\text{ light}}$, which was systematically larger for Conv galaxies than for Free galaxies due to the smoothing of the flux. For LT galaxies, the half-particle-light radii are overestimating the half-mass radii from EAGLE, meaning it has ongoing star forming events along the disc. For HT galaxies, the half-particle-light radii and the half-mass radii have a 1-1 relationship while $R_{1/2\text{ light part.}}$ underestimates $R_{1/2\text{ light}}$, meaning the mock observing process is adding a bias in the observation which only occurs for HT galaxies potentially due to the difference age and stellar distribution. HT galaxies also have a larger number of older stellar particles and have, on average, less ordered rotation according to its κ_{co} value. Using light-weighted parameters, therefore, can add uncertainty to the recovery of the stellar mass of a galaxy, which vary with respect to the type of galaxy observed.

- We extracted the stellar kinematics from the mock observations using GIST, and compared the rotation curves for both the mock galaxies and the EAGLE galaxies placed edge-on. Looking at a single slit at the major axis of rotation, we found that there is a great variety in the amount of deviation seen between EAGLE and the mocks. Although some galaxies match the profile and, overall, we do not see either an overestimation or underestimation of the curves, there is still a large scatter in the data as a result of specific galaxies which do not follow this trend. Some of this scatter can be attributed to substructure within the galaxies, which is lost when binning the data at an SNR threshold and adding PSF convolution to model seeing conditions. However, since the process of binning the data into pixels and averaging over the slit width was replicated from the mocks, some of these errors should have been mitigated. In that case, we looked at the differences between the LT and HT galaxies, where HT galaxies have less ordered rotation which affect the fit of the spectral lines and have a larger dispersion. As a result, HT galaxies have a larger scatter and level of overestimation compared to LT galaxies, which leads to uncertainties in the rotation curves of spheroidal galaxies

- When comparing our results of the maximum velocity and the fiducial velo-

city with those seen in Oman et al. (2015), we do not find a clear difference between the LT and the HT galaxies, mainly because the maximum rotation velocity of the galaxy is reached by looking at the gas, not the stars. However, this study has shown that while some galaxies are able to replicate the maximum velocities from the EAGLE data, others can deviate due to the extent of the rotation curve or due to large uncertainties. We find discrepancies in the mock observations versus the simulations, meaning there is still work to be done in fixing these issues before these mock observations can be a trustworthy comparison. With this in mind, the results show that there are many parameters to consider when making mock observations, such as determining the radii at which comparisons are being drawn accurately since using light-weighted radii can lead to vast overestimations in the velocities, in particular for galaxies less disc-like. This difference is also mass-dependent, where more massive galaxies with a longer radial extent fully fit within the aperture of the mocks, and sufficient stellar particles lie within the slit used to extract the rotation curves. Therefore, both curves extend as far as each other, leading to fewer discrepancies between the fiducial and maximum velocities.

- Some previous studies of mock observations look at particular galaxies rather than large samples; however, as we have shown, specific galaxies can match the simulations accurately. There is still a large scatter in the data as a result of the diversity of rotation curves extracted. This can be a result of multiple parameters: GIST could be misinterpreting the data since we do not include gas in the making of the mock data cubes. Since GIST relies on spectral fitting through SSP templates to extract the kinematics, signature lines used as fits could be missing from the cubes, therefore leading to larger discrepancies in the derived line-of-sight velocities. Additionally, we are comparing 3D particle data with 2D data, which can lead to uncertainties in the projection. The PSF convolution process could be removing some substructure and hence affecting the derived spectrum. Overall, there are multiple parameters to consider to improve the process of making mock observations, but as more studies and pipelines are tested and created, we will be able to do higher-level comparisons.

4.1 Future Work

This work was developed as a base for the future use of mock observations. Here, we have carried out checks to ensure the reliability of SimSpin in creating mock observations and GIST's ability to process these mock IFU cubes. We looked at

the stellar kinematics of a sample of dwarf galaxies; however, from these mock cubes, it is also possible to explore multiple other parameters, such as their stellar age and metallicity distribution. These, similarly, can be compared with the input data from EAGLE. Burger et al. (2022) studied the stellar age and metallicity distribution of simulated galaxies from AREPO (Springel, 2010) and the way it can trace the dark matter distribution. Doing a similar comparison with our mock data and simulated data could determine if the properties of the galaxies as a whole (not only their kinematics) have dissimilarities from the properties from simulations. The next stage for this research would be to extract the dark matter density profiles from the rotation curves and compare them with those from the simulations.

Additionally, adding gas particle data to make the mock observations would result in a more rounded perspective on the actual profile of the galaxies. Gas extends out further and, hence, traces the dark matter mass distribution better; however, a comparison between the mock observations of gas versus stars would enable us to differentiate the role of each component. This could also be done by testing data from other simulations since they use different stellar feedback prescriptions and sub-grid physics, which would allow the discernment of the role of each parameter. Similarly, using the EAGLE runs at a higher star formation gas density threshold could show how the programs used here deal with a more unrealistic galaxy.

In this age where observational instruments are constantly achieving higher resolutions and simulations are resolving smaller scales, the need to compare these two is growing. Here we have studied one of the many ways that this can be achieved and demonstrated the potential of combining Integral Field Spectroscopy with hydrodynamical simulations to improve our understanding of the structures of galaxies and the dark matter within them.

Bibliography

Abril-Melgarejo, V., Epinat, B., Mercier, W., et al. 2021, , 647, A152, doi: 10.1051/0004-6361/202038818

Allington-Smith, J., Murray, G., Content, R., et al. 2002, , 114, 892, doi: 10.1086/341712

Bacon, R., Copin, Y., Monnet, G., et al. 2001, , 326, 23, doi: 10.1046/j.1365-8711.2001.04612.x

Bacon, R., Accardo, M., Adjali, L., et al. 2010, in Society of Photo-Optical Instrumentation Engineers (SPIE) Conference Series, Vol. 7735, Ground-based and Airborne Instrumentation for Astronomy III, ed. I. S. McLean, S. K. Ramsay, & H. Takami, 773508, doi: 10.1117/12.856027

Baldry, I. K., Driver, S. P., Loveday, J., et al. 2012, , 421, 621, doi: 10.1111/j.1365-2966.2012.20340.x

Behroozi, P. S., Wechsler, R. H., & Conroy, C. 2013, , 770, 57, doi: 10.1088/0004-637X/770/1/57

Benítez-Llambay, A., Frenk, C. S., Ludlow, A. D., & Navarro, J. F. 2019, , 488, 2387, doi: 10.1093/mnras/stz1890

Bittner, A., Falcón-Barroso, J., Nedelchev, B., et al. 2019, GIST: Galaxy IFU Spectroscopy Tool, Astrophysics Source Code Library, record ascl:1907.025. http://ascl.net/1907.025

Bouché, N., Carfantan, H., Schroetter, I., Michel-Dansac, L., & Contini, T. 2015, GalPaK 3D: Galaxy parameters and kinematics extraction from 3D data, Astrophysics Source Code Library, record ascl:1501.014. http://ascl.net/1501.014

Bouché, N. F., Bera, S., Krajnović, D., et al. 2022, , 658, A76, doi: 10.1051/0004-6361/202141762

Bower, R. G., Schaye, J., Frenk, C. S., et al. 2017, , 465, 32, doi: 10.1093/mnras/stw2735

Bruzual, G., & Charlot, S. 2003, , 344, 1000, doi: 10.1046/j.1365-8711.2003.06897.x

Bullock, J. S., & Boylan-Kolchin, M. 2017, , 55, 343, doi: 10.1146/annurev-astro-091916-055313

Bundy, K., Bershady, M. A., Law, D. R., et al. 2015, , 798, 7, doi: 10.1088/0004-637X/798/1/7

Burger, J. D., Zavala, J., Sales, L. V., et al. 2022, , 513, 3458, doi: 10.1093/mnras/stac994

Cappellari, M. 2017, , 466, 798, doi: 10.1093/mnras/stw3020

Cappellari, M., & Copin, Y. 2003, , 342, 345, doi: 10.1046/j.1365-8711.2003.06541.x

Cappellari, M., & Emsellem, E. 2004, , 116, 138, doi: 10.1086/381875

Chung, H., Park, C., & Park, Y.-S. 2021, , 257, 66, doi: 10.3847/1538-4365/ac2828

Cid Fernandes, R., Mateus, A., Sodré, L., Stasińska, G., & Gomes, J. M. 2005, , 358, 363, doi: 10.1111/j.1365-2966.2005.08752.x

Correa, C. A., Schaye, J., Clauwens, B., et al. 2017, , 472, L45, doi: 10.1093/mnrasl/slx133

Davis, M., Efstathiou, G., Frenk, C. S., & White, S. D. M. 1985, , 292, 371, doi: 10.1086/163168

de Graaff, A., Trayford, J., Franx, M., et al. 2022, , 511, 2544, doi: 10.1093/mnras/stab3510

den Brok, M., Carollo, C. M., Erroz-Ferrer, S., et al. 2020, , 491, 4089, doi: 10.1093/mnras/stz3184

Di Teodoro, E. M., & Fraternali, F. 2015, , 451, 3021, doi: 10.1093/mnras/stv1213

Dolag, K., Borgani, S., Murante, G., & Springel, V. 2009, , 399, 497, doi: 10.1111/j.1365-2966.2009.15034.x

Dutton, A. A., Buck, T., Macciò, A. V., et al. 2020, , 499, 2648, doi: 10.1093/mnras/staa3028

Dutton, A. A., Macciò, A. V., Buck, T., et al. 2019, , 486, 655, doi: 10.1093/mnras/stz889

Einstein, A., & de Sitter, W. 1932, Contributions from the Mount Wilson Observatory, 3, 51

Emsellem, E., Cappellari, M., Krajnović, D., et al. 2011, , 414, 888, doi: 10.1111/j.1365-2966.2011.18496.x

Falcón-Barroso, J., Bacon, R., Bureau, M., et al. 2006, , 369, 529, doi: 10.1111/j.1365-2966.2006.10261.x

Fattahi, A., Navarro, J. F., Sawala, T., et al. 2016, , 457, 844, doi: 10.1093/mnras/stv2970

Fitts, A., Boylan-Kolchin, M., Elbert, O. D., et al. 2017, , 471, 3547, doi: 10.1093/mnras/stx1757

Flores, H., Hammer, F., Puech, M., Amram, P., & Balkowski, C. 2006, , 455, 107, doi: 10.1051/0004-6361:20054217

Gadotti, D. A., Sánchez-Blázquez, P., Falcón-Barroso, J., et al. 2019, , 482, 506, doi: 10.1093/mnras/sty2666

Garrison-Kimmel, S., Rocha, M., Boylan-Kolchin, M., Bullock, J. S., & Lally, J. 2013, , 433, 3539, doi: 10.1093/mnras/stt984

González Delgado, R. M., García-Benito, R., Pérez, E., et al. 2015, , 581, A103, doi: 10.1051/0004-6361/201525938

Guérou, A., Krajnović, D., Epinat, B., et al. 2017, , 608, A5, doi: 10.1051/0004-6361/201730905

Guidi, G., Casado, J., Ascasibar, Y., et al. 2018, , 479, 917, doi: 10.1093/mnras/sty1480

Harborne, K. 2019, SimSpin: Kinematic analysis of galaxy simulations, Astrophysics Source Code Library, record ascl:1903.006. http://ascl.net/1903.006

Ho, I. T., Medling, A. M., Groves, B., et al. 2016, , 361, 280, doi: 10.1007/s10509-016-2865-2

Jahn, E. D., Sales, L. V., Marinacci, F., et al. 2021, arXiv e-prints, arXiv:2110.00142. https://arxiv.org/abs/2110.00142

Kelz, A., Verheijen, M. A. W., Roth, M. M., et al. 2006, , 118, 129, doi: 10.1086/497455

Kendrew, S., Zieleniewski, S., Houghton, R. C. W., et al. 2016, , 458, 2405, doi: 10.1093/mnras/stw438

Koleva, M., Prugniel, P., Bouchard, A., & Wu, Y. 2009, , 501, 1269, doi: 10.1051/0004-6361/200811467

Larson, R. B. 1974, , 169, 229, doi: 10.1093/mnras/169.2.229

Lazar, A., Bullock, J. S., Boylan-Kolchin, M., et al. 2020, , 497, 2393, doi: 10.1093/mnras/staa2101

Le Fèvre, O., Vettolani, G., Garilli, B., et al. 2005, , 439, 845, doi: 10.1051/0004-6361:20041960

Leroy, A. K., Hughes, A., Schruba, A., et al. 2016, , 831, 16, doi: 10.3847/0004-637X/831/1/16

Li, C., & White, S. D. M. 2009, , 398, 2177, doi: 10.1111/j.1365-2966.2009.15268.x

Ludlow, A. D., Bose, S., Angulo, R. E., et al. 2016, , 460, 1214, doi: 10.1093/mnras/stw1046

McConnell, N. J., & Ma, C.-P. 2013, , 764, 184, doi: 10.1088/0004-637X/764/2/184

Moore, B. 1994, , 370, 629, doi: 10.1038/370629a0

Nanni, L., Thomas, D., Trayford, J., et al. 2022, , 515, 320, doi: 10.1093/mnras/stac1531

Navarro, J. F., Eke, V. R., & Frenk, C. S. 1996, , 283, L72, doi: 10.1093/mnras/283.3.L72

Navarro, J. F., Frenk, C. S., & White, S. D. M. 1997, , 490, 493, doi: 10.1086/304888

Navarro, J. F., Hayashi, E., Power, C., et al. 2004, , 349, 1039, doi: 10.1111/j.1365-2966.2004.07586.x

Nelson, D., Pillepich, A., Genel, S., et al. 2015, Astronomy and Computing, 13, 12, doi: 10.1016/j.ascom.2015.09.003

Nelson, D., Springel, V., Pillepich, A., et al. 2019, Computational Astrophysics and Cosmology, 6, 2, doi: 10.1186/s40668-019-0028-x

Oman, K. A., Navarro, J. F., Fattahi, A., et al. 2015, , 452, 3650, doi: 10.1093/mnras/stv1504

Ostriker, J. P., Peebles, P. J. E., & Yahil, A. 1974, , 193, L1, doi: 10.1086/181617

Peirani, S., Sonnenfeld, A., Gavazzi, R., et al. 2019, , 483, 4615, doi: 10.1093/mnras/sty3475

Planck Collaboration, Aghanim, N., Akrami, Y., et al. 2020, , 641, A6, doi: 10.1051/0004-6361/201833910

Pontzen, A., & Governato, F. 2012, , 421, 3464, doi: 10.1111/j.1365-2966.2012.20571.x

Price, S. H., Kriek, M., Feldmann, R., et al. 2017, , 844, L6, doi: 10.3847/2041-8213/aa7d4b

Roberts, M. S., & Rots, A. H. 1973, , 26, 483

Rogstad, D. H., Lockhart, I. A., & Wright, M. C. H. 1974, , 193, 309, doi: 10.1086/153164

Roper, F. A., Oman, K. A., Frenk, C. S., et al. 2022, arXiv e-prints, arXiv:2203.16652. https://arxiv.org/abs/2203.16652

Sánchez, S. F., García-Benito, R., Zibetti, S., et al. 2016a, , 594, A36, doi: 10.1051/0004-6361/201628661

Sánchez, S. F., Pérez, E., Sánchez-Blázquez, P., et al. 2016b, , 52, 171. https://arxiv.org/abs/1602.01830

Santos-Santos, I. M. E., Navarro, J. F., Robertson, A., et al. 2020, , 495, 58, doi: 10.1093/mnras/staa1072

Sarzi, M., Falcón-Barroso, J., Davies, R. L., et al. 2006, , 366, 1151, doi: 10.1111/j.1365-2966.2005.09839.x

Sawala, T., Frenk, C. S., Fattahi, A., et al. 2016, , 457, 1931, doi: 10.1093/mnras/stw145

Schaye, J., Crain, R. A., Bower, R. G., et al. 2015, , 446, 521, doi: 10.1093/mnras/stu2058

Scott, N., van de Sande, J., Croom, S. M., et al. 2018, , 481, 2299, doi: 10.1093/mnras/sty2355

Shen, S., Madau, P., Conroy, C., Governato, F., & Mayer, L. 2014, , 792, 99, doi: 10.1088/0004-637X/792/2/99

Shen, S., Mo, H. J., White, S. D. M., et al. 2003, , 343, 978, doi: 10.1046/j.1365-8711.2003.06740.x

Smee, S. A., Gunn, J. E., Uomoto, A., et al. 2013, , 146, 32, doi: 10.1088/0004-6256/146/2/32

Springel, V. 2010, , 401, 791, doi: 10.1111/j.1365-2966.2009.15715.x

Springel, V., White, S. D. M., Tormen, G., & Kauffmann, G. 2001, , 328, 726, doi: 10.1046/j.1365-8711.2001.04912.x

Thatte, N. A., Clarke, F., Bryson, I., et al. 2014, in Society of Photo-Optical Instrumentation Engineers (SPIE) Conference Series, Vol. 9147, Ground-based and Airborne Instrumentation for Astronomy V, ed. S. K. Ramsay, I. S. McLean, & H. Takami, 914725, doi: 10.1117/12.2055436

Tiley, A. L., Swinbank, A. M., Harrison, C. M., et al. 2019, , 485, 934, doi: 10.1093/mnras/stz428

Tyson, J. A., Valdes, F., & Wenk, R. A. 1990, , 349, L1, doi: 10.1086/185636

van der Marel, R. P., & Franx, M. 1993, , 407, 525, doi: 10.1086/172534

Vazdekis, A., Koleva, M., Ricciardelli, E., Röck, B., & Falcón-Barroso, J. 2016, , 463, 3409, doi: 10.1093/mnras/stw2231

Vogelsberger, M., Genel, S., Springel, V., et al. 2014, , 444, 1518, doi: 10.1093/mnras/stu1536

Westfall, K. B., Cappellari, M., Bershady, M. A., et al. 2019, , 158, 231, doi: 10.3847/1538-3881/ab44a2

Zieleniewski, S., Thatte, N., Kendrew, S., et al. 2015, , 453, 3754, doi: 10.1093/mnras/stv1860

Zwicky, F. 1933, Helvetica Physica Acta, 6, 110

Appendix A

A.1 Appendix

The sample of selected galaxies described in Sect. 2.2 are shown in Figs. A.1, A.2, A.3, for the LT galaxies, and A.4, A.5 for HT. With the velocity map output from GIST on the left, the rotation curves in the middle, and the EAGLE particle velocities on the right. The colors and descriptions are the same as Chap. 3.

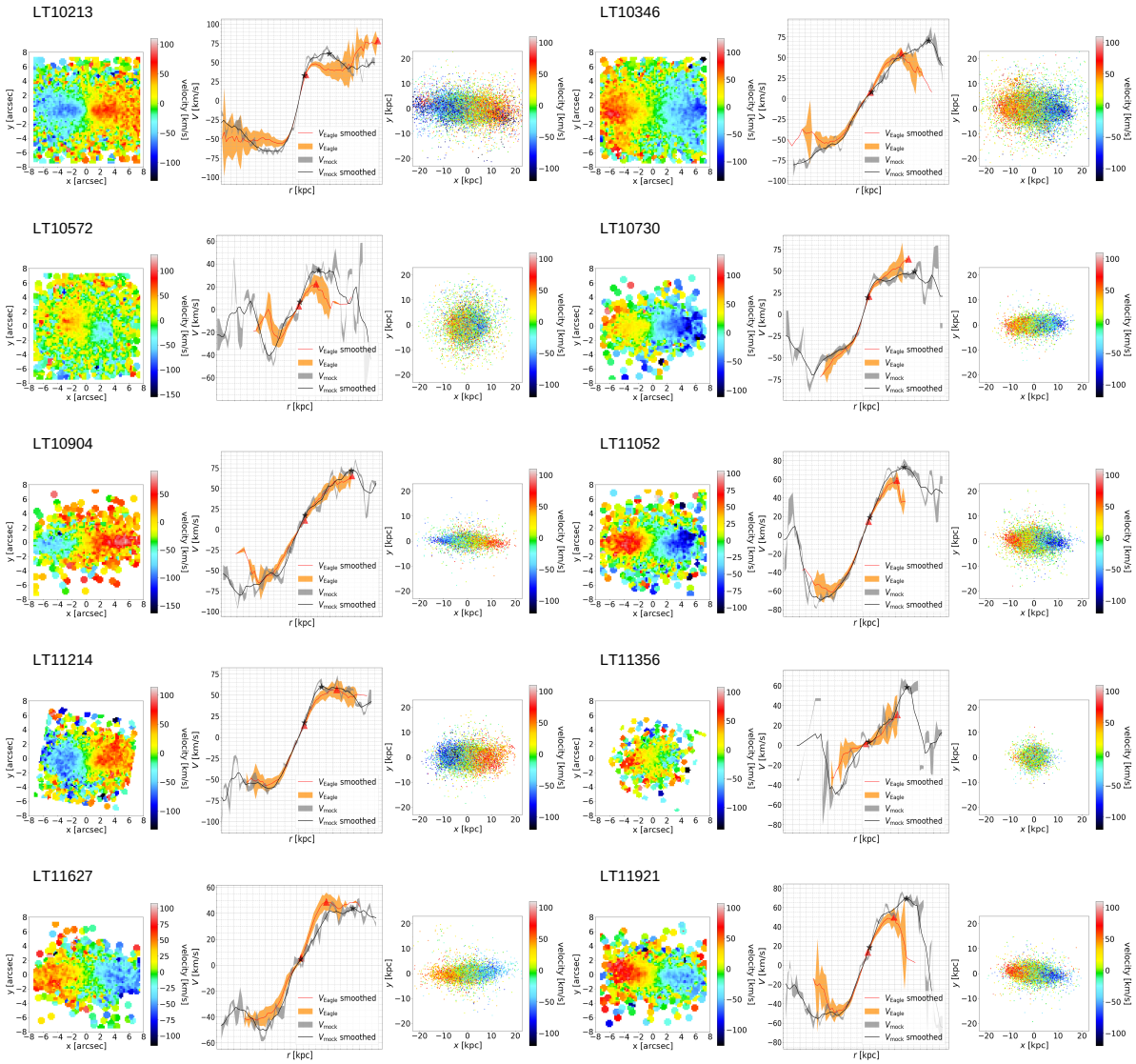

Figure A.1: Same as Fig. 3.2 but for the remainder of our LT sample.

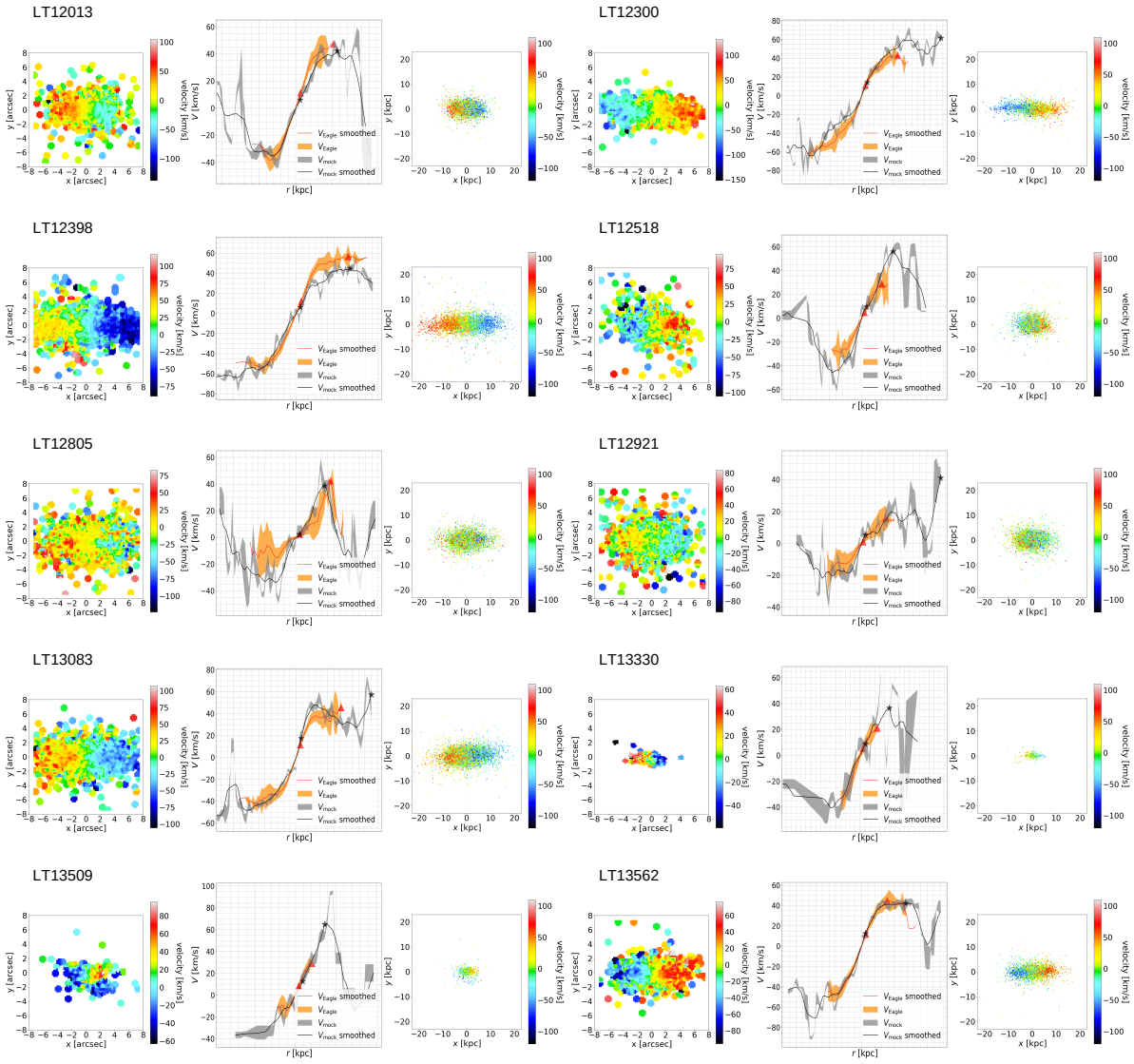

Figure A.2: Same as Fig. 3.2 but for the remainder of our LT sample.

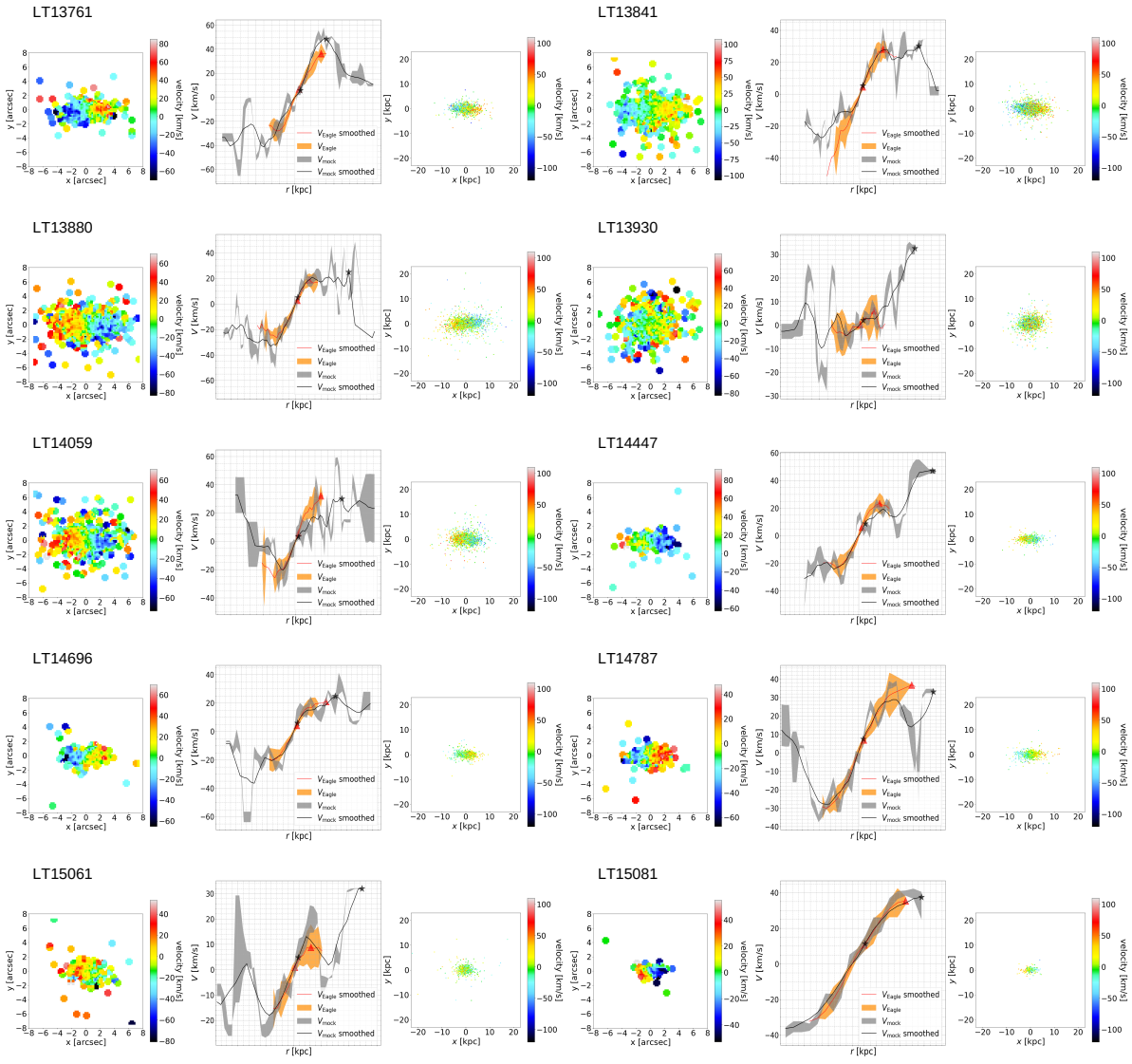

Figure A.3: Same as Fig. 3.2 but for the remainder of our LT sample.

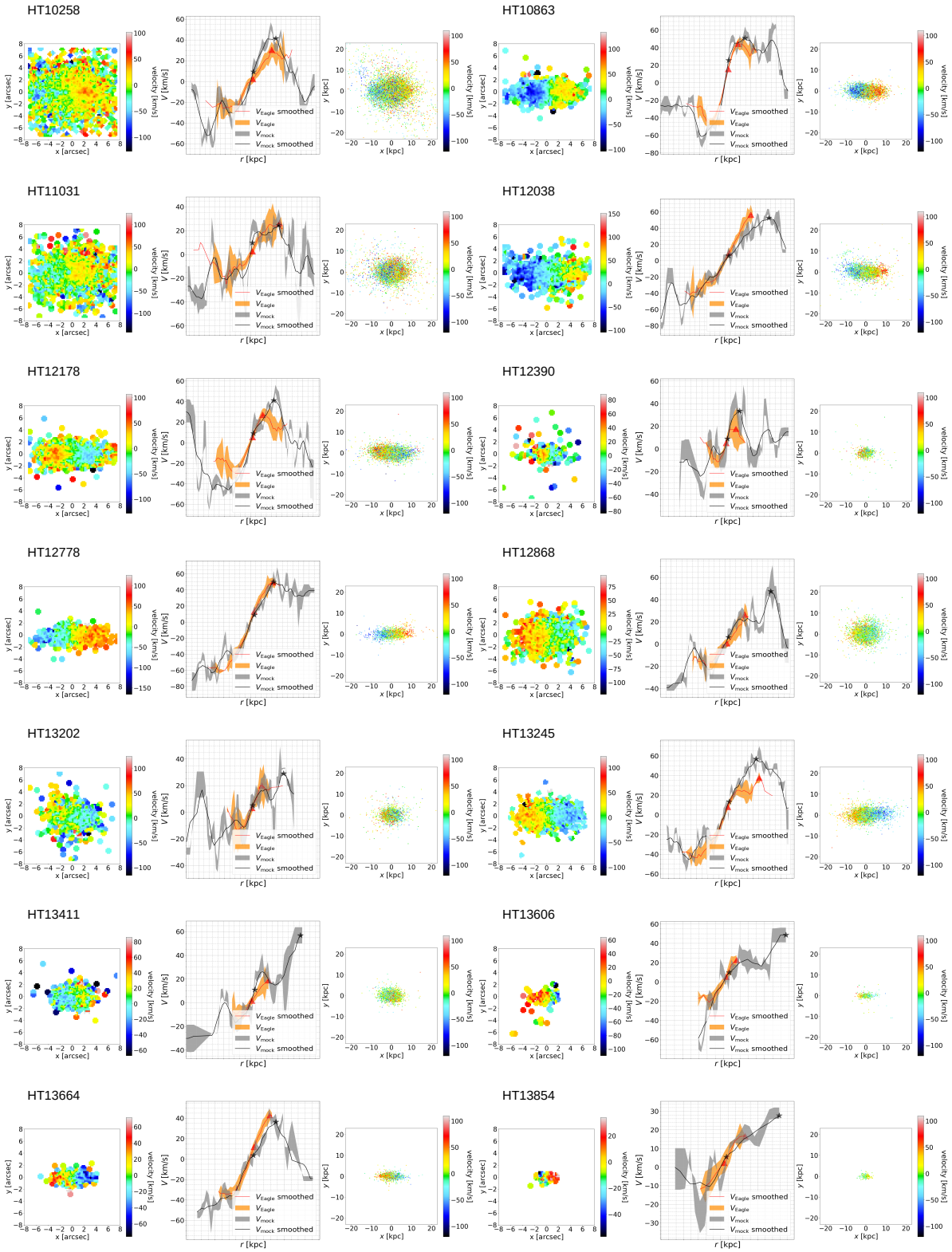

Figure A.4: Same as Fig. 3.2 but for the remainder of our HT sample.

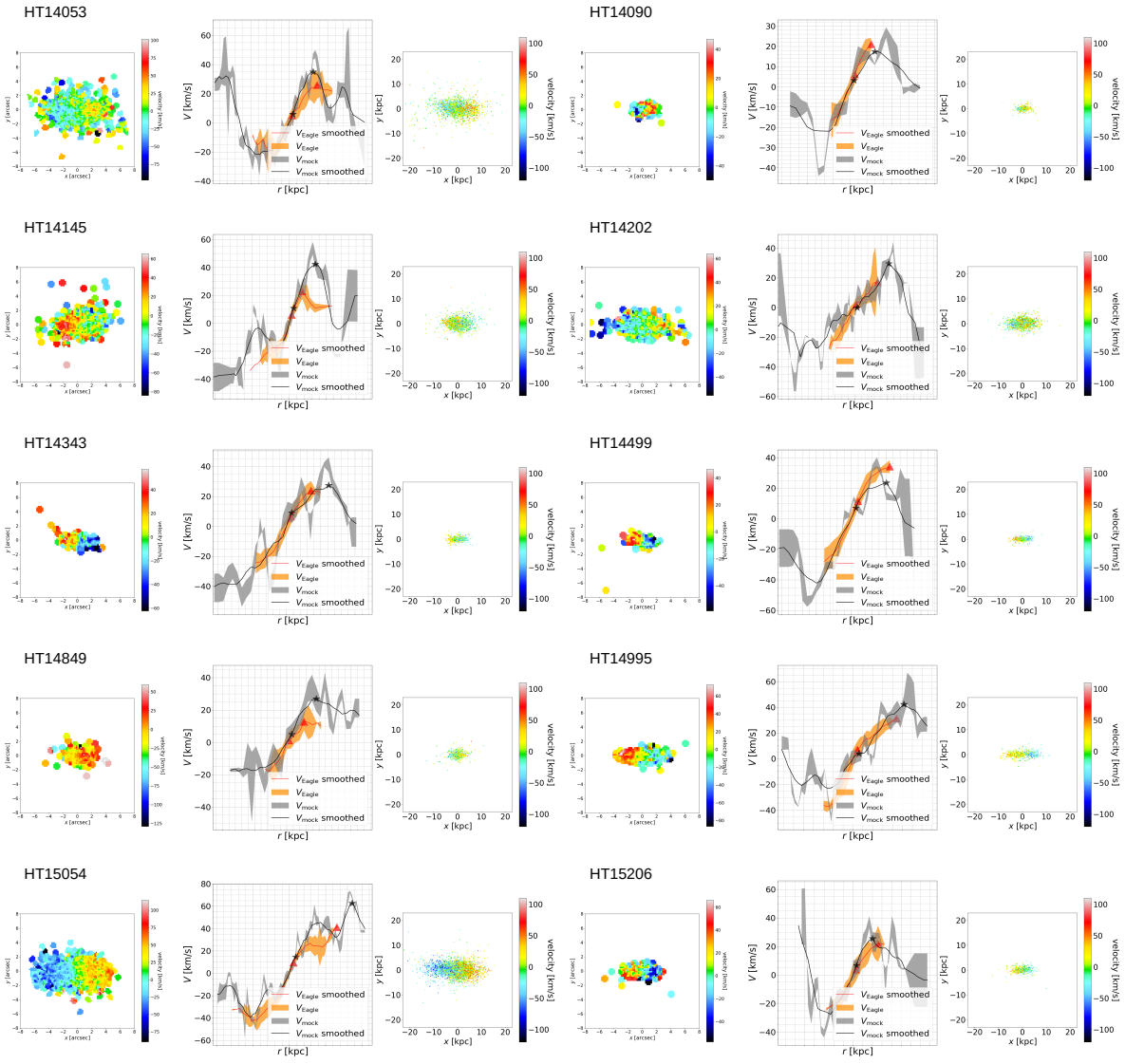

Figure A.5: Same as Fig. 3.2 but for the remainder of our HT sample.

Colophon

This thesis is based on a template developed by Matthew Townson and Andrew Reeves. It was typeset with LaTeX 2_ε. It was created using the *memoir* package, maintained by Lars Madsen, with the *madsen* chapter style. The font used is Latin Modern, derived from fonts designed by Donald E. Kunith.